EUROPEAN ORGANIZATION FOR NUCLEAR RESEARCH

CERN–PPE/93–11
13. 01. 1993

Antiproton-proton annihilation at rest into two-body final states

C. Amsler[13], D.S. Armstrong[1], I. Augustin[7], C.A. Baker[4], B.M. Barnett[10], C.J. Batty[4], K. Beuchert[2], P. Birien[1], J. Bistirlich[1], P. Blüm[7], R. Bossingham[1], H. Bossy[1], K. Braune[11], J. Brose[10], D.V. Bugg[8], M. Burchell[5], T. Case[1], S.U. Chung[10,a], A. Cooper[8], K.M. Crowe[1], H.P. Dietz[11], S. v. Dombrowski[13], M. Doser[5], W. Dünnweber[11], D. Engelhardt[7], M. Englert[11], M.A. Faessler[11], C. Felix[11], G. Folger[11], R. Hackmann[10], R.P. Haddock[9], F.H. Heinsius[6], N.P. Hessey[5], P. Hidas[3], P. Illinger[11], D. Jamnik[11,b], Z. Jávorfi[3], H. Kalinowsky[10], B. Kämmle[6], T. Kiel[6], J. Kisiel[11,c], E. Klempt[10], M. Kobel[5], H. Koch[2], C. Kolo[11], K. Königsmann[11], M. Kunze[2], R. Landua[5], J. Lüdemann[2], H. Matthaey[2], M. Merkel[10,d], J.P. Merlo[10], C.A. Meyer[13], U. Meyer-Berkhout[11], L. Montanet[5], A. Noble[13], F. Ould-Saada[13], K. Peters[2], G. Pinter[3], S. Ravndal[2], J. Salk[2], A.H. Sanjari[8], E. Schäfer[10], B. Schmid[13], P. Schmidt[6], S. Spanier[10], C. Straßburger[10], U. Strohbusch[6], M. Suffert[12], D. Urner[13], C. Völcker[11], F. Walter[10], D. Walther[2], U. Wiedner[6], N. Winter[7], J. Zoll[5], Č. Zupančič[11].

The Crystal Barrel Collaboration

1) University of California, LBL, Berkeley, CA 94720, USA
2) Universität Bochum, D-4630 Bochum, Germany
3) Academy of Science, H-1525 Budapest, Hungary
4) Rutherford Appleton Laboratory, Chilton, Didcot OX11 0QX, UK
5) CERN, CH-1211 Genève, Switzerland
6) Universität Hamburg, D-2000 Hamburg, Germany
7) Universität Karlsruhe, D-7500 Karlsruhe, Germany
8) Queen Mary and Westfield College, London E1 4NS, UK
9) University of California, Los Angeles, CA 90024, USA
10) Universität Mainz, D-6500 Mainz, Germany
11) Universität München, D-8000 München, Germany
12) Centre de Recherches Nucléaires, F-67037 Strasbourg, France
13) Universität Zürich, CH-8001 Zürich, Switzerland
a) On leave of absence from BNL, Upton, NY
b) On leave of absence from the University of Ljubljana, Ljubljana, Slovenia
c) On leave of absence from the University of Silesia, Katowice, Poland
d) Part of this work appears in the PhD thesis of M. Merkel

EUROPEAN ORGANIZATION FOR NUCLEAR RESEARCH

Abstract

We report measurements of branching ratios for production of a series of two meson final states in $\bar{p}p$ annihilations at rest in liquid hydrogen. We find:

$$
\begin{aligned}
BR(\bar{p}p \to \pi^+\pi^-) &= (3.07 \pm 0.13) \cdot 10^{-3} & BR(\bar{p}p \to \eta\eta) &= (1.64 \pm 0.10) \cdot 10^{-4} \\
BR(\bar{p}p \to K^+K^-) &= (0.99 \pm 0.05) \cdot 10^{-3} & BR(\bar{p}p \to \eta\omega) &= (1.51 \pm 0.12) \cdot 10^{-2} \\
BR(\bar{p}p \to \pi^0\pi^0) &= (6.93 \pm 0.43) \cdot 10^{-4} & BR(\bar{p}p \to \eta\eta') &= (2.16 \pm 0.25) \cdot 10^{-4} \\
BR(\bar{p}p \to \pi^0\eta) &= (2.12 \pm 0.12) \cdot 10^{-4} & BR(\bar{p}p \to \omega\omega) &= (3.32 \pm 0.34) \cdot 10^{-2} \\
BR(\bar{p}p \to \pi^0\omega) &= (5.73 \pm 0.47) \cdot 10^{-3} & BR(\bar{p}p \to \omega\eta') &= (0.78 \pm 0.08) \cdot 10^{-2} \\
BR(\bar{p}p \to \pi^0\eta') &= (1.23 \pm 0.13) \cdot 10^{-4}
\end{aligned}
$$

These are the first measurements of the channels $\eta\eta'$ and $\omega\eta'$ and in almost all the other channels are more precise than previous results. We also obtain, in a more precise fashion, the following ratios of branching ratios: $K^+K^-/\pi^+\pi^- = 0.323 \pm 0.013$, $\pi^0\eta'/\pi^0\eta = 0.548 \pm 0.056$, $\eta\eta'/\eta\eta = 1.31 \pm 0.15$, $\omega\eta'/\omega\eta = 0.515 \pm 0.040$, $\pi^0\eta/\pi^0\pi^0 = 0.303 \pm 0.010$, $\eta\eta/\pi^0\pi^0 = 0.232 \pm 0.011$ and $\pi^0\omega/\eta\omega = 0.377 \pm 0.012$. The measurements are made for different η and η' decays, and we thus obtain $\Gamma_{\eta \to 3\pi^0}/\Gamma_{\eta \to \gamma\gamma} = 0.841 \pm 0.034$, and $\Gamma_{\eta' \to \gamma\gamma}/\Gamma_{\eta' \to \pi^0\pi^0\eta} = 0.091 \pm 0.009$.

Submitted to Zeit. für Physik C

1 Introduction

The process of antiproton–proton ($\bar{p}p$) annihilation is – in spite of continued efforts – far from being understood. Not even general agreement on the basic dynamical questions has so far been achieved: can the process be understood in the conventional picture of mesons and baryons [1], or is a description in terms of quarks and gluons more appropriate [2] ? If the latter is the case, is annihilation dominated by two–body intermediate states [3] ? And what is the role of initial state [4, 5] and final state [6] interactions ? Is there a dominance of rearrangement diagrams or annihilation diagrams [7] ? Can the $q\bar{q}$ annihilation vertex be described by an effective one–gluon operator [8] or does the $q\bar{q}$ pair annihilate into many gluons carrying vacuum quantum numbers [9] ? Is annihilation governed by phase space [10], or is SU(3) symmetry at work [11] ?

Apart from these theoretical difficulties there is also a shortage of precise and reliable data. In the late 1960's $\bar{p}p$ annihilation was investigated in bubble chamber experiments. However, owing to their nature, bubble chamber experiments are limited to the analysis of reactions with, at most, one neutral pion in the final state. Yet some 60% of the annihilations produce two or more π^0's or η's, and specific channels such as $\bar{p}p \to \eta\omega$ (which is important for testing annihilation models) remained unmeasured. Further, the decays proceed from an *a priori* unknown mixture of initial angular momentum states of the $\bar{p}p$ system. Recently, the Asterix collaboration (with an electronic detector) improved upon this situation by determining branching ratios for $\bar{p}p$ annihilation at rest from initial S- and P-wave states separately [12–17]. But that experiment was also restricted to, at most, one neutral pion in the final state. Two experiments have been carried out searching for π^0 [18, 19] and η [20, 21] mesons produced inclusively in $\bar{p}p$ annihilations. Both experiments yielded information on two–body reactions, but some of their results are statistically not very significant, and the results of the two experiments often disagree.

The Crystal Barrel detector has been designed to overcome the limitations of these previous experiments; it is an electronic detector capable of measuring both charged and neutral annihilation products with high efficiency and large solid angle coverage. Data from the detector have so far been used in studies of meson spectroscopy[22, 23], with the aim of searching for glueballs or hybrids. In this paper we turn our attention to the questions raised above concerning the nature of the $\bar{p}p$ annihilations. We report on determinations of branching ratios for the following reactions (where the $\bar{p}p$ annihilation occurs at rest in liquid hydrogen):

$\bar{p}p \to \pi^+\pi^-$	$\bar{p}p \to \eta\eta$
$\bar{p}p \to K^+K^-$	$\bar{p}p \to \eta\omega$
$\bar{p}p \to \pi^0\pi^0$	$\bar{p}p \to \eta\eta'$
$\bar{p}p \to \pi^0\eta$	$\bar{p}p \to \omega\omega$
$\bar{p}p \to \pi^0\omega$	$\bar{p}p \to \omega\eta'$
$\bar{p}p \to \pi^0\eta'$	

Annihilation into two mesons is restricted by conservation laws: parity P, C–parity, and angular momenta are strictly conserved in strong interaction processes. Since the $\bar{p}p$ wave function contains both isospin components $I = 0$ and $I = 1$ (with $I_3 = 0$), G–parity cannot be used to derive further selection rules.

In $\bar{p}p$ interactions at rest only a limited number of partial waves contribute to annihilation. In spectroscopic notation, these states are the $^{(2S+1)}L_J = {}^1S_0$, ${}^3S_1$, ${}^1P_1$, ${}^3P_0$, ${}^3P_1$ and ${}^3P_2$ states (where S is the spin of the $\bar{p}p$ atom, L its orbital angular momentum

and J the total angular momentum). Annihilation into $\pi^0\pi^0$, $\pi^0\eta$, $\eta\eta$, $\pi^0\eta'$ or $\eta\eta'$ is forbidden from S–states, but allowed from the $^3P_0$ and $^3P_2$ states of the $\bar{p}p$ system (with respectively an orbital angular momentum $l = 0$ or 2 between the two outgoing mesons). The states $^3S_1$ and $^1P_1$ states may contribute to annihilations into $\pi^0\omega$, $\eta\omega$ and $\omega\eta'$. The orbital angular momenta are then $l = 1$ and $l = 0$, respectively. Annihilation into $\pi^+\pi^-$ and K^+K^- is permitted from the $^3P_0$, $^3P_2$ and $^3S_1$ states. Production of two ω mesons may proceed via all ^3P_J states and the $^1S_0$ state. These constraints must be borne in mind when interpreting the results.

2 General features of the apparatus and data

2.1 The Crystal Barrel detector

The experiment is carried out on an external beam line at the CERN Low Energy Antiproton Ring (LEAR). Figure 1 shows a side view of the Crystal Barrel detector. The data presented in this paper were obtained with a 200 MeV/c beam of antiprotons incident on a liquid hydrogen (LH_2) target positioned at the centre of the detector. The antiprotons slow down in the LH_2 and annihilate at rest. The target is surrounded by a detector which sits in a large solenoidal magnet providing a uniform axial 1.5T field. Charged particles are seen first in two cylindrical Proportional Wire Chambers (PWC's) which surround the target (main axis, identical to the beam direction z). The inner/outer PWC covers 99%/97% of 4π in the laboratory frame (as seen from the centre of the target). The PWC's are surrounded in turn by a cylindrical Jet Drift Chamber (JDC) which provides most of the charged tracking capability. The JDC has 23 layers of wires radially (r), and is divided into 30 sectors around the beam pipe (ϕ). Charge division provides the z coordinates of hits along each wire (accurate to 2%, 8 mm). A track can be reconstructed from a minimum of 3 hits, giving a maximum coverage of 93% of 4π in the laboratory frame. The JDC is surrounded by an electromagnetic (EM) calorimeter consisting of 1380 CsI crystals. The crystals are arranged (with a projective geometry) in 26 rings along the z (beam) direction, and 60 rows in ϕ (except in the first three and last three z layers where space constraints only permit 30 rows). Each crystal subtends 6 by 6 degrees as seen from the centre of the target (except in z layers 1-3 and 23-26 which subtend 6 by 12 degrees). The σ of the EM energy resolution of the calorimeter is typically 2.5% at 1 GeV. Full details of the apparatus are given elsewhere [24].

The analysis is based on five data sets taken in four run periods in 1989 and 1990. One data set was taken with an *open trigger* where the detector was read out every time we observed an antiproton in beam position counters just in front of the target. The other data sets were taken with a *zero-prong* trigger requiring no hits in the two PWC's (in addition to an incident antiproton); thus this data is restricted to events with only photons in the final state. The branching ratios for reactions $\bar{p}p \to \pi^0\pi^0$, $\bar{p}p \to \pi^+\pi^-$ and $\bar{p}p \to K^+K^-$ are determined from *open trigger* data. The other branching ratios are derived from *zero–prong trigger* data.

2.2 Event reconstruction

The detector provides information on charged particles in the JDC and on neutral particles in the CsI barrel calorimeter. Figure 2 shows a typical event with two tracks and two photons (corresponding to the process $\bar{p}p \to \pi^+\pi^-\pi^0$). When reconstructing events we start with the JDC. We search in the $r - \phi$ projection for hits in adjacent layers and combine them into track elements. These elements are considered full tracks if a circle can

be fit to the hits in the $r-\phi$ projection. The z information on the hits is then combined into the track via a fit of a helix to the track's trajectory [25].

Photons lead to showers in the crystal barrel which extend over up to 30 crystals. In the first step in finding showers, we search for all contiguous clusters of crystals with energy deposits of more than 1 MeV per crystal. If, inside a cluster, there is only one local maximum in the energy, then the cluster is called a single shower (and the shower energy equals the sum of the individual crystal energies). If there are several (n) local maxima, then the total cluster energy is partitioned into n shower energies according to :

$$E^i_{\rm shower} = \frac{E^i_9}{\sum_{i=1}^{n} E^i_9} \cdot E_{\rm cluster} \qquad (1)$$

where E^i_9 is the sum of energies over the 3x3 crystal matrix centered on the crystal with the local maximum. To be called a shower a minimum total energy of 20MeV is required. The position of a shower is calculated from the mean of the crystal positions weighted with the energy deposits. When more than one shower is present in a cluster, then the position of each shower is taken to be the center of the crystal with the local maximum energy deposit.

In events containing charged tracks, the track can pass through the calorimeter; in which case it will give a shower–like signal. These are recognized in the analysis by extrapolating each track's JDC trajectory to the calorimeter, and suppressing any spatially coincident shower. The remaining showers are considered photons.

For photons the measured shower energy needs to be corrected for energy losses (which depend on the energy and on θ, the angle to the beam direction). Therefore the energies are multiplied with correction factors determined from a Monte Carlo calculation (typical magnitude of correction is 5%).

In the analysis described below, events having photons with an impact point on one of the crystals surrounding the entrance/exit holes of the barrel are rejected. This reduces the azimuthal solid angle to 95%, but avoids energy leakage of a shower out of the barrel.

2.3 Detection and reconstruction efficiencies

The performance of the detector is modelled by Monte Carlo (MC) simulation. The MC is based on the program package GEANT [26]. MC data are reconstructed with the same analysis programs as real data, applying the same cuts and kinematic fits. The errors for the kinematic fit were adjusted separately for each channel and run period. This is achieved by a comparison of MC and real data events, with the aim of obtaining the same number of produced events in real data for confidence level cuts at 5%, 10% and 20%.

2.4 Identification of neutral mesons

Most of the branching ratios reported in this paper are derived from $\bar{\rm p}$p annihilations into neutral particles. Therefore we describe here in some detail the reduction of the data to final states with a well defined number of photons.

In order to obtain data samples of annihilations without charged particles in the final state, the following method is used: the events are reconstructed and any with charged particles are rejected. This removes over 95% of events in the *open trigger* data set, and also rejects 20% of the *zero-prong* trigger data. The latter occurs because, even with fully efficient PWC's in the trigger rejecting charged track events on-line, some events with charged tracks can satisfy the 'no PWC hit' trigger. These events include: when a second antiproton entered the target within the active time of the data acquisition (pile-up),

Table 1: Momenta for $\bar{p}p$ annihilations into two mesons.

Channel		Momentum	Channel		Momentum
$\bar{p}p \rightarrow$	$\pi^+\pi^-$	927.8 MeV/c	$\bar{p}p \rightarrow$	$\eta\eta$	761.0 MeV/c
	K^+K^-	797.9 MeV/c		$\eta\omega$	656.4 MeV/c
	$\pi^0\pi^0$	928.5 MeV/c		$\eta\eta'$	546.1 MeV/c
	$\pi^0\eta$	852.3 MeV/c		$\omega\omega$	518.5 MeV/c
	$\pi^0\omega$	768.4 MeV/c		$\omega\eta'$	350.5 MeV/c
	$\pi^0\eta'$	658.7 MeV/c			

tracks from K^0_S mesons with long decay paths, pair production in material outside of the PWC's, and tracks in the outer layers of the JDC from charged particles created by interactions in the barrel and scattered back into the JDC. The resulting sample of events is called *all–neutral* data. The number of observed photons in an *all-neutral* event is not necessarily equal to the number produced in the annihilation: photons may be lost due to the limited solid angle or due to the photon energy cut at 20MeV. Additional photons may appear to be present due to fluctuations in the showering process; thus one photon can manifest itself in the calorimeter as two neighbouring showers (5% probability).

As the next step we impose energy and momentum conservation by the following cuts:

$$\begin{aligned} 1500MeV < \quad E_{\rm tot} &\leq 2000MeV \\ |\vec{p}_{\rm tot}| &\leq 300MeV/c \end{aligned} \tag{2}$$

Events which do not satisfy these constraints arise from a variety of reasons. These include events with missing photons, events containing a K^0_L which is either not observed or interacts with a low energy deposit in the calorimeter, events with an antiproton scattered into the barrel and pile-up events.

The surviving events are then subject to a 4C kinematical fit (total energy and the three momentum components are conserved), hypothesis $\bar{p}p \rightarrow n\gamma$, n being the observed number of photons. We require a fit probability of at least 10%.

2.5 Tagging of π^0 and η mesons

Once an $n\gamma$ event has been selected as above, the nature of the reaction has to be established. For two-body production from a fixed centre-of-mass energy (the antiproton annihilations occur at rest in the laboratory) each combination of meson types (e.g. $\pi^0\pi^0$, $\pi^0\eta$, etc.) is characterized by a fixed meson momentum. In Table 1 we list the momenta for all reactions studied in this paper. To establish the presence of a reaction in our data we thus study the meson momentum distributions. These are obtained either by looking at the two-photon momentum distribution for all combinations of two-photons in an event, or by carrying out kinematic fits with constraints on total energy and momentum plus extra constraints of, as appropriate, π^0 or η mass(es) (decaying to two photons) and then examining the momentum distribution of the π^0 or η. Signal strengths are found by fits of a Gaussian plus (appropriate) polynomial background. For most reactions we make the measurements in more than one $n\gamma$ final state, reflecting different decays of the mesons.

As a test that we are correctly establishing signal strengths, we find the strength for one reaction ($\bar{p}p \rightarrow \pi^0\eta$) using several different methods. We measure $\bar{p}p \rightarrow \pi^0\eta$ using both the 4- and 8γ final states. We began with the 4γ final state ($\eta \rightarrow \gamma\gamma$). Method a) looked at the momentum spectrum for all pairs of photons. Method b) required a 5C kinematic

fit to $\bar{p}p \to \pi^0\gamma\gamma$, followed by inspection of the π^0 momentum spectrum. Method c) used a similar 5C kinematic fit to $\bar{p}p \to \eta\gamma\gamma$, and counted signal events in the η momentum spectrum. We next looked at the 8γ final state ($\eta \to \pi^0\pi^0\pi^0$). Method d) applied a χ^2 test to all two-photon combinations in the events. This test looks for pairs of photons with an invariant mass close to that of π^0 or η and forms a χ^2 using the error on the mass (found from the energy and directional errors on the photons). The test checks all possible two-photon permutations making use of all photons in the event. The permutation with the minimum χ^2 is identified as the reaction type. If an event is of the type $\bar{p}p \to \pi^0\pi^0\pi^0\pi^0$, we study the π^0 momentum spectrum as usual. Method e) is to apply an 8C kinematic fit to the hypothesis $\bar{p}p \to \pi^0\pi^0\pi^0\pi^0$. Once again we extract the $\bar{p}p \to \pi^0\eta$ signal strength by studying the π^0 momentum spectrum. To find the number of $\bar{p}p \to \pi^0\eta$ events produced we take the signal strength found by each method (Table 2), correct for any intermediate decay branching ratios, and scale by the analysis efficiency (found from Monte Carlo). The results of the five methods have an average of 23,880 produced events, with a $\chi^2/n_{\rm dof}$ of 2.3/4 (we ignore possible correlations between the data sets). The good consistency of the results (from both the 4γ and the 8γ final states) illustrates our ability to understand both the detector and the analysis methods.

Table 2: Number of produced $\pi^0\eta$ events determined by use of five different methods (see text). Given are the number of observed events, the geometrical reconstruction efficiency (not including π^0 and η decay branching fractions) and the number of produced events.

Method	Observed events	Efficiency	Produced events
a)	3878 ± 98	0.445 ± 0.021	22,680 ± 1310
b)	3904 ± 159	0.437 ± 0.022	23,240 ± 1530
c)	4180 ± 174	0.444 ± 0.023	24,490 ± 1630
d)	1162 ± 64	0.148 ± 0.007	25,820 ± 1960
e)	1043 ± 50	0.139 ± 0.007	24,600 ± 1740

3 The *open trigger* data

We study the reactions $\bar{p}p \to \pi^+\pi^-$, $\bar{p}p \to K^+K^-$ and $\bar{p}p \to \pi^0\pi^0$ in the *open trigger* data set with 4.382 million events.

3.1 Vertex reconstruction and annihilation in flight

Since we wish to measure branching ratios for annihilations at rest on LH_2, we need to ensure that all the data correspond to these conditions. Accordingly we study the vertex distribution (along the beam axis) in a random sub-sample of the reconstructed open trigger events (see Figure 3). We find that $(3.9 \pm 0.7)\%$ of events are associated with structure outside the LH_2, mostly at -6cm, the position of the entrance beam counters. We also observe an asymmetry in the vertex distribution in Figure 3. This is associated with annihilations occurring in-flight as the antiproton beam passes through the LH_2 before it stops. By fitting the vertex distribution we find $(5.7 \pm 1.1)\%$ of events are due to this effect. As a check, we parameterize measurements of proton energy loss in LH_2 [27] and combine this with an extrapolation (down to zero momentum) of the antiproton annihilation cross-section found above 180MeV/c [28]. We predict that approximately 4% of the incident antiprotons should annihilate in flight; in agreement with the measured value.

In all branching ratio calculations, we correct the antiproton flux for these two sources of annihilations not occurring at rest on LH_2.

3.2 The reactions $\bar{p}p \to \pi^+\pi^-$ and $\bar{p}p \to K^+K^-$

The first step in this study was to reduce the raw (un-reconstructed) data set to a manageable size. Therefore we searched the data for event topologies compatible with two back-to-back (collinear) charged tracks. The criteria were: between 15 and 60 hits in the JDC (we require long tracks for good momentum resolution), that only two clusters of hit JDC sectors are permitted, that the two clusters of sectors be opposite each other (forcing collinearity in the $r-\phi$ projection), and that the sum of the charge on all hit wires be the same at each end of the JDC (forcing collinearity in the orthogonal $r-z$ projection). This selected 116,155 events which were fully reconstructed.

The efficiency of this selection for retaining collinear events was found by reconstructing 1 million random events and carrying out the full analysis to be described below. The fraction of the collinear content of this sample which also survives the data reduction constraints just described, is $(89 \pm 3)\%$.

To find the collinear signals in reconstructed data we required the events to contain only two good tracks, where 'good' implies that a track starts in the inner five JDC layers and that it extends out to at least layer 10 (reducing the geometric acceptance per track, but greatly improving momentum resolution). No other tracks are permitted in the inner 10 layers. However, extra tracks are accepted in the outer JDC layers, as these can arise from low momentum charged particles back–scattered from interactions in the calorimeter. The two good tracks were required to have a common opening angle at the target of greater than 170 degrees (ensuring collinearity). This selected 29,925 candidate collinear events. To find the collinear signals, we fit a single track to the combined set of hits from both good tracks in an event. The distribution of the momentum of this single track in each event (which has a resolution approximately five times better than that of the shorter individual tracks) is shown in Figure 4(a) (one entry per event). Clear collinear signals are seen, corresponding to the reactions $\bar{p}p \to K^+K^-$ and $\bar{p}p \to \pi^+\pi^-$.

By tightening the collinearity requirement, and imposing on the data that there be no other activity in the calorimeter other than that for two minimum ionizing tracks, we can eliminate almost all of the background shown. If we further require that the tracks span all layers of the JDC we also improve the momentum resolution. The result after these requirements is shown in Figure 4(b). With these conditions we obtain a measure of the JDC momentum resolution for a track spanning the whole JDC diameter, of 2.2% at 928MeV/c. However, due to the reduction in statistics and unknown systematic effects associated with the cut on calorimeter activity, these events are not suitable for branching ratio measurements. We therefore measure the branching ratios using the data in Figure 4(a). This is fit with a background term (cubic polynomial) plus a Gaussian for each collinear signal. We find that there are 2615 $\bar{p}p \to K^+K^-$ events and 8138 $\bar{p}p \to \pi^+\pi^-$ events. Repeating the fit with different starting values for each coefficient and different assumptions for the background shape gives a 1% variation in the signal strengths.

To check that the signals arise from annihilations at rest on the LH_2, we would normally study the z vertex distribution. However, due to their collinear nature, no unique definition of the vertex exists for the selected two track events. We thus study the distribution of the z coordinates of the single track fit in each event at its closest approach to the beam direction. This shows no structure for events occurring outside the LH_2, but it does give an asymmetry of $(0.8 \pm 0.9)\%$, a possible indication of in–flight annihilations

Table 3: Absolute branching ratios for reactions measured in the *open trigger* data (the first error is purely statistical, the second systematic; the combined error is given on previous measurements).

Reaction	Our Branching Ratio	Previous Measurements
$BR(\bar{p}p \to K^+K^-)$	$(0.99 \pm 0.03 \pm 0.04) \cdot 10^{-3}$	$(1.1 \pm 0.1) \cdot 10^{-3}$ [29]
		$(0.96 \pm 0.08) \cdot 10^{-3}$ [30]
		$(0.99 \pm 0.10) \cdot 10^{-3}$ [31]
$BR(\bar{p}p \to \pi^+\pi^-)$	$(3.07 \pm 0.04 \pm 0.12) \cdot 10^{-3}$	$(3.2 \pm 0.3) \cdot 10^{-3}$ [29]
		$(3.3 \pm 0.4) \cdot 10^{-3}$ [30]
		$(3.1 \pm 0.3) \cdot 10^{-3}$ [31]
$BR(\bar{p}p \to \pi^+\pi^-) \to \pi^0\pi^0$	$(6.93 \pm 0.22 \pm 0.37) \cdot 10^{-4}$	$(4.8 \pm 1.0) \cdot 10^{-4}$ [32]
		$(6 \pm 4) \cdot 10^{-4}$ [33]
		$(1.4 \pm 0.3) \cdot 10^{-4}$ [34]
		$(2.06 \pm 0.14) \cdot 10^{-4}$ [19]
		$(2.5 \pm 0.3) \cdot 10^{-4}$ [18]

contaminating the selected data set (this is corrected for when calculating the branching ratios).

We make a final correction to allow for losses in the signals due to pile-up of events in the detector. This can occur if the antiproton which triggered the event is immediately preceeded or followed by a second antiproton. We record a flag during data-taking if a second antiproton enters the target within 10μsec of the trigger antiproton. We find that 1.61% of all *open trigger* events are affected. Looking at the selected collinear events we find that only 0.85% have the pile–up flag set. The difference has a 6σ significance, so we correct the calculated branching ratios accordingly.

To calculate the branching ratios of these signals we estimate the efficiency of the analysis using MC simulations. We generate MC signals for both channels and subject the reconstructed MC data to the same analysis as real data. We find that the acceptance for $\bar{p}p \to K^+K^-$ is $(74.4 \pm 1.1)\%$, and $(75.0 \pm 0.7)\%$ for $\bar{p}p \to \pi^+\pi^-$. To obtain the full efficiency for finding collinear signals in our data, we have to combine the acceptance with the factor of $(89 \pm 3)\%$ for the data reduction described earlier.

We check that the MC reproduces the data correctly, by seeing that the MC acceptance scales with the observed signal strengths as the analysis criteria are varied. The main deviation occurs as the minimum track length is increased from 10 to 23 layers. This introduces an error of 1.2% . Part of this is due to statistical effects, but it also reflects how well reconstructed MC events match real data, so it is included in the systematic error on all calculations.

Combining these efficiencies and corrections with the observed signal strengths we find the branching ratios given in Table 3. In this table the first error quoted is statistical (allowing for fluctuations in both the signal and the background) and the second systematic (found by adding in quadrature all the errors quoted above). Removing all the contributions in common to both measurements gives the ratio $BR(\bar{p}p \to K^+K^-)/BR(\bar{p}p \to \pi^+\pi^-) = (0.323 \pm 0.011 \pm 0.007)$, where again the first error is statistical and the second systematic. As can be seen, these results are fully compatible with, and of higher accuracy than, previous measurements.

3.3 The reaction $\bar{p}p \to \pi^0\pi^0$

For this reaction we started with the same data set as previously, but then reduced it by removing all events with the pile-up flag set, and events in which a signal was found in a crystal which was known to have a large fluctuating noise level; reducing the number of useful events to 3.605 million. Correcting by $-(5.7 \pm 1.1)\%$ to account for in-flight annihilations, and by $-(3.9 \pm 0.7)\%$ for antiprotons not stopping in the target, gives a total of (3.267 ± 0.043) million $\bar{p}p$ annihilations at rest in liquid hydrogen.

The *all-neutral* selection criteria described earlier select 131,222 events, 5985 of which have four detected photons. After the 4C kinematic fit $\bar{p}p \to 4\gamma$, 1653 events survive a probability cut at 10% and are further analysed.

Figure 5 shows the momentum distribution of any pair of two photons in these events. A peak is observed at the expected momentum of 928.5 MeV/c. It contains 1112 ± 34 events, where the error reflects the statistical uncertainty and the fit error (note that each $\pi^0\pi^0$ event gives two entries in the signal peak). The width σ_p of the distribution (after a 4C fit) is 2.2 MeV/c. Using a larger sample of $\pi^0\pi^0$ events (found in the *zero-prong* trigger data) we check for in-flight contributions to the observed signal strength. We select events as before and carry out a 5C fit to $\bar{p}p \to \pi^0\pi^0$, where the two π^0 masses are fixed, $p_x = p_y = 0$, and p_z and the antiproton energy are constrained to conserve total energy. The distribution of p_z in the events gives (at most) an inflight contribution to the signal of $(0.6 \pm 0.6)\%$. Accordingly we correct the number of $\pi^0\pi^0$ by $-(0.6 \pm 0.6)\%$.

In Figure 6 we display the γ angular distribution in π^0 decays. The angle is calculated in the π^0 rest frame between the γ momentum and the π^0 direction of flight in the laboratory. The fall in acceptance at small and large angles corresponds to events with asymmetric γ energies in the laboratory frame. Such a loss is expected since the minimum γ energy occurring in this reaction is 4.8 MeV, and there is an analysis cut on low energy γ's of 20MeV. The otherwise flat distribution indicates the excellent uniform acceptance of the detector. Also shown (superimposed) is the same distribution in MC events after analysis. The good agreement is clear.

The detection efficiency for $\pi^0\pi^0$ events is determined by MC simulations to be $\epsilon_{\pi^0\pi^0} = 0.488 \pm 0.010$. The error represents the statistical uncertainty. Systematic studies of the reliability of the efficiency give an error of 5.2% . This is determined as follows:

a) Reconstruction errors:
Since kinematic fits are carried out in the analysis, it is necessary that the photon energy and direction error distributions are equally well known in MC and data. The distributions of the difference in energy and angle between reconstructed and kinematically fitted events agree well for MC and real data, leading to similar confidence level distributions. By varying the error distributions in MC events we find a variation of the detection efficiency of 1.8%.

b) Target position:
For *all-neutral* data we are unable to determine accurately the event vertex position. We thus vary the Monte Carlo annihilation vertex by 5 mm (the vertex precision) around the nominal vertex position in the beam direction. This shift changes the detection efficiency, and hence the branching ratio, by 3% .

c) Statistics:
The statistical error of the MC simulation is always smaller than 1.8% (except for $X\eta'$ in 4γ, where it is 2.3%)

d) Geometry:
To avoid problems with shower energy leakage out of the barrel, we normally exclude

events with photon impact points in the crystal rings next to the entrance and exit holes of the barrel. To check that this is sufficient we also exclude the second and third neighbouring crystal rings. We find a variation of the branching ratio of 1.6%.

e) 10MeV threshold instead of 20MeV:
We impose a minimum shower energy cut of 20MeV during the analysis. This energy threshold was changed to 10MeV. We find a 3% variation in the branching ratio. The main effects of lowering the threshold are to decrease the number of lost photons and to increase the number of split–off showers. This latter effect is dominant, paradoxically leading to a lower efficiency (due to incomplete split–off recognition).

With the statistical error of 3.1% in the number of $\pi^0\pi^0$ events, an analysis error of 5.2%, an error of 0.7% from the vertex distribution, and an error of 1.5% for the fraction of antiprotons (and of 0.6% for the fraction of $\pi^0\pi^0$) annihilating in flight, we obtain the branching ratio given in Table 3. It can be seen that this result is larger than the several previous measurements. However, since we fully reconstruct the events, have a large detector acceptance with a high statistics signal and understand well the $\bar{p}p$ annihilation rate (as witnessed by the good agreement of the collinear branching ratios with previous measurements), we feel that our result is accurate.

3.4 Branching ratios for annihilation into $\pi^+\pi^-$ and K^+K^- in LH_2 from the $^3S_1$ initial state

Remembering that $\bar{p}p$ annihilation in $\pi^0\pi^0$ can only proceed from the $^3P_0$ and $^3P_2$ initial states, the large value for this rate implies a sizable P wave contribution to the $\pi^+\pi^-$ channel. Scaling our result for $BR(\bar{p}p \to \pi^0\pi^0)$ by the appropriate Clebsch Gordon factor of 2, we obtain that the branching ratio for annihilation into $\pi^+\pi^-$ from the P state in LH_2 is $BR_P(\bar{p}p \to \pi^+\pi^-) = (1.39 \pm 0.09) \cdot 10^{-3}$. The difference of $(1.68 \pm 0.16) \cdot 10^{-3}$ from the total $\pi^+\pi^-$ rate is the amount which proceeds from the $^3S_1$ initial state (Table 4). We thus find that the S and P initial states contribute 55% and 45%, respectively, to the total $\pi^+\pi^-$ rate in LH_2.

Table 4: Absolute branching ratios for the S-wave contribution to $\bar{p}p$ annihilation into $\pi\pi$ and $K\bar{K}$.

Reaction	Branching Ratio	
$\bar{p}p \to \pi^+\pi^-$	$(1.68 \pm 0.13) \cdot 10^{-3}$	
$\bar{p}p \to K^+K^-$	$(0.91 \pm 0.02) \cdot 10^{-3}$	
$\bar{p}p \to K^0_S K^0_L$	$(0.83 \pm 0.05) \cdot 10^{-3}$	[13]

The branching ratio into $\pi^+\pi^-$ from the 2P states has been determined in a previous experiment [12] to be $BR_{2P}(\bar{p}p \to \pi^+\pi^-) = (4.81 \pm 0.49) \cdot 10^{-3}$. Assuming that all P–wave annihilations occur at the same rate as those from only the 2P–states, we can define the fraction of P–wave annihilation in LH_2 as $f_P = BR_P/BR_{2P}$. We find $f_P = (28.9 \pm 3.5)\%$ in LH_2. This result appears to contradict earlier estimates, e.g. [12] which obtained $(8.6 \pm 1.1)\%$. However, this is because of the value of $BR(\bar{p}p \to \pi^0\pi^0)$ used by previous authors. The larger value of f_P that we find is thus attributable to our new measurement of $BR(\bar{p}p \to \pi^0\pi^0)$.

The large $\pi^0\pi^0$ branching ratio thus apparently challenges the widely held view that $\bar{p}p$ annihilation at rest proceeds dominantly from S wave. However, the above interpretation does assume that in LH_2, the branching ratio for annihilation into $\pi^+\pi^-$ is

indcpendent of the principal quantum number (n) of the $\bar{p}p$ system. We discuss this result further in a separate letter [35], where we present the results in the light of an atomic cascade model of antiprotonic hydrogen after formation of the atom in highly excited states.

For the channel K^+K^- we cannot derive the S and P wave contributions in the same way. For example, the process $\bar{p}p \rightarrow K^0_S K^0_L$ proceeds only from initial S-wave, however it does so with an *a priori* unknown mixture of isospin 0 and 1, and cannot therefore be scaled to give the S-wave rate into K^+K^-. Accordingly we proceed by making the naive assumption that the fraction f_P is the same for K^+K^- as for $\pi^+\pi^-$. This implies that $(28.9 \pm 3.5)\%$ of the branching ratio into K^+K^- from the 2P states contributes to annihilations in LH_2. The branching ratio K^+K^- from the 2P states has been measured [12] as $(0.29 \pm 0.05) \cdot 10^{-3}$. After subtraction of $(28.9 \pm 3.5)\%$ of the latter value from our measurement for $BR(\bar{p}p \rightarrow K^+K^-)$, we find a branching ratio into K^+K^- from S states of $(0.91 \pm 0.02) \cdot 10^{-3}$ (Table 4). In Table 4 we also give the branching ratio for $K^0_S K^0_L$. The amplitudes for these two processes have a different dependence on the isospin 0 and 1 amplitudes, i.e. $A(K^+K^-) = (A_1 - A_0)/\sqrt{2}$ and $A(K^0\overline{K^0}) = (A_1 + A_0)/\sqrt{2}$. That the two processes have a near equal rate implies that in S-wave either isospin 0 or 1 is dominant.

4 The *zero-prong* trigger data

The *zero-prong* data is subject to the basic *all-neutral* requirements described earlier. Below we describe the details of the analyses leading to observation of specific signals in the data. The data used were obtained in 4 different run periods. Since the detector performance can vary with time, each analysis is carried out separately on each data set. The resulting signal strengths are then summed, with the errors added as independent Gaussian errors. When figures are given showing the data, they are from just one run period to illustrate data quality (with the fit to the signal shown inset). The MC efficiencies are also found separately in each data set (to correctly model detector performance). The combined efficiency for any reaction is thus the value from each run period averaged together, weighted by the antiproton flux for that period. The antiproton flux is in all cases determined by extracting the $\pi^0\pi^0$ content of the data and normalizing using the $BR(\bar{p}p \rightarrow \pi^0\pi^0)$ measured above. For each analysis the total observed signal strength, average efficiency and total antiproton flux is given in Table 6. Note that for final states containing $X\eta'$, the smallest two data sets contained statistically insignificant signals. They were therefore not included in the analysis of these channels.

4.1 The four-photon final state ($\pi^0\pi^0$, $\pi^0\eta$, $\pi^0\eta'$, $\eta\eta$ and $\eta\eta'$)

The 4γ final state is dominated by $\bar{p}p \rightarrow \pi^0\pi^0$. This is shown in Figure 7(a). The fit to the data in the momentum range for the reaction is displayed inset. Also seen is a smaller peak due to the reaction $\bar{p}p \rightarrow \pi^0\eta$, seen better in Figure 7(b) which excludes the $\pi^0\pi^0$ peak (the fit to the data is again shown inset).

The momenta for the two reactions $\bar{p}p \rightarrow \eta\eta$ and $\bar{p}p \rightarrow \pi^0\omega$ are rather close, and both reactions contribute to the 4γ final state. In the latter annihilations a low-energy photon from $\omega \rightarrow \pi^0\gamma$ may be lost, the 4C fit then detunes the kinematics slightly and the π^0 momenta are shifted, obscuring the weak signal from $\bar{p}p \rightarrow \eta\eta$ events. In our data (Figure 7(b)) we indeed see an asymmetric structure at about 760MeV/c. The background from $\pi^0\omega$ is eliminated by requiring both $\gamma\gamma$ pairs to have a mass of more than 200 MeV/c^2 (Figure 7(c)); an undistorted signal due to $\bar{p}p \rightarrow \eta\eta$ is now clearly visible.

For $\bar{p}p \to \pi^0\eta'$ and $\eta\eta'$, we again use the 4γ final state and select $\gamma\gamma$ pairs with an invariant mass compatible with a π^0. We plot in Figure 7(d) the π^0 momentum distribution showing three peaks (note that the expected $\pi^0\pi^0$ signal is out of the momentum range shown): $\pi^0\eta$ (the signal for which is so strong it passes off the vertical scale of the histogram), then $\pi^0\omega$ follows (with a lost photon), finally there is a small peak from $\pi^0\eta'$. The inset shows an expanded view of the π^0 momentum distribution in the region where the signal from $\pi^0\eta'$ is expected. By similarly plotting the η momentum spectrum we observe $\bar{p}p \to \eta\eta'$ jointly with $\pi^0\eta$, $\eta\eta$, and $\eta\omega$ (Figure 7(e)).

4.2 The five-photon final state ($\pi^0\omega$, $\eta\omega$ and $\omega\eta'$)

The reactions $\bar{p}p \to \pi^0\omega$, $\eta\omega$, and $\omega\eta'$ are studied in the 5γ data. We select events which satisfy a 5C kinematic fit to the hypothesis $\bar{p}p \to \pi^0\gamma\gamma\gamma$. The $\pi^0\gamma$ invariant mass distribution in these events contains a strong ω signal. Using the χ^2 method (section 2.5) we divide the data into three samples: Class A is compatible with the hypothesis $\pi^0\pi^0\gamma$, class B with $\pi^0\eta\gamma$ and class C contains events which do not satisfy either hypothesis.

We plot in Figure 8(a) the π^0 momentum in the class A sample, in Figure 8(b) the η momentum in the class B sample, and in Figure 8(c) the momentum of the $\gamma\gamma$ pair in class C events when the recoiling $\gamma\pi^0$ pair has an invariant mass compatible with that of an ω (700 to 860MeV/c^2). The class A events give a striking peak due to $\bar{p}p \to \pi^0\omega$. In class B there is a clear signal for $\eta\omega$ at the expected momentum. In the class C sample we see four peaks. These represent $\bar{p}p$ annihilations into $\omega\eta'$, $\omega\omega$ with one photon lost, $\eta\omega$ and $\pi^0\omega$ (where the η or the π^0 hypothesis was incorrectly rejected because of a poor χ^2). The fit to the $\omega\eta'$ signal is shown inset.

4.3 The six-photon final state ($\omega\omega$)

We search for $\bar{p}p \to \omega\omega$ in the 6γ data set. Events are selected in which no η's and exactly two neutral pions are identified. These events are kinematically fit to the hypothesis $\bar{p}p \to \pi^0\pi^0\gamma\gamma$ (6C fit with the usual constraints on energy and momentum plus the two extra constraints of the π^0 mass). We select $\gamma\pi^0$ combinations compatible with the ω mass (to within $\pm$ 80MeV/c^2) and then study the mass of the recoiling $\gamma\pi^0$ pair (Figure 9). This also contains an ω signal, and we count the number of events with two fully reconstructed ω mesons. This is the only channel where this approach is used. The reason for not counting the signal strength in the ω momentum spectrum is a poorly defined background under the signal, which would introduce a correspondingly large systematic error. From the fit shown in Figure 9 we obtain that in this analysis at the ω mass we have a Gaussian mass resolution with σ of 16MeV/c^2. If we use the same data with just a 4C kinematic fit balancing energy and momentum, we again observe the ω in the $\gamma\pi^0$ invariant mass distribution, this time with a Gaussian mass resolution with σ of 23MeV/c^2.

4.4 The eight–photon final state ($\pi^0\eta$, $\pi^0\eta'$, $\eta\eta$ and $\eta\eta'$)

The 8γ events are kinematically fit to three hypotheses: (A) $\pi^0\pi^0\pi^0\pi^0$, (B) $\pi^0\pi^0\pi^0\eta$ and (C) $\pi^0\pi^0\eta\eta$. Events with a probability of more than 10% are retained (the number of events satisfying more than one hypothesis is negligible). The π^0 momentum distribution of class (A) events is shown in Figure 10(a) (4 entries per event), and of class (B) in Figure 10(b) (3 entries per event). The two distributions show peaks originating from the reactions $\bar{p}p \to \pi^0\eta$ and $\pi^0\eta'$ respectively. The number of events is determined from a fit (see insets). The reactions $\bar{p}p \to \eta\eta$ and $\eta\eta'$ are observed by plotting the η momentum distribution of class (B) and class (C) events (Figures 10(c) and 10(d) respectively).

4.5 The nine-photon final state ($\eta\omega$ and $\omega\eta'$)

The 9γ events are kinematically fit to the $4\pi^0\gamma$ and to the $3\pi^0\eta\gamma$ hypotheses. Figures 11(a,b) show the momentum distributions of ω candidates for these two respective channels with peaks at momenta corresponding to $\eta\omega$ and $\omega\eta'$ annihilations. The insets show fits to expanded views of the data.

4.6 Error analysis

The accuracy of the analysis on each channel is assumed to be the same as that for $\pi^0\pi^0$. We have checked for all channels that the branching ratios do not depend on the confidence level (c.l.) cut; the variation of results cutting at 5%, 10%, or 20% c.l. is described by the error of 1.8% given for the $\pi^0\pi^0$ case. The cut on geometry was tested on the channels $\pi^0\omega$ and $\eta\omega$, again with the same result as in the $\pi^0\pi^0$ case. Since we normalize the antiproton flux using the $\pi^0\pi^0$ branching fraction and the magnitude of this signal in each data set, the errors on these quantities are combined into the systematic error on branching ratios.

As already stated, the *zero-prong* data presented herein were obtained in four different data-taking periods. Between these periods the detector may have been moved, maintenance work carried out, the target conditions changed, extra counters placed in the beam line, the trigger conditions changed slightly, the beam quality varied, and so on. Accordingly we analyzed the data independently in each run period (details are given elsewhere [36]). The results in all periods are compatible. We illustrate this here by comparing the results for BR($\bar{p}p \to \pi^0\eta$) (in the 4γ final state) in all four periods. The signal was found as described above. The MC efficiency was calculated separately for each period (allowing for slightly different calorimeter energy resolution etc). We use the $\bar{p}p$ annihilation rates as found from the $\pi^0\pi^0$ signal in each period. The resulting branching ratios are given in Table 5, where the error given is only that of the $\pi^0\eta$ signal statistics. An unweighted average of the four results is also given, along with the r.m.s. spread of the sample. This spread is of equivalent magnitude to the statistical errors, indicating that any systematic differences are small, of magnitude 2% or 3%. This is in line with our estimate of 5.2% as the total analysis systematic error (which does not include the error from the $\bar{p}p$ annihilation rate). This total error is larger than the few percent we estimate here because it not only includes effects between data-taking periods, but also those common to all results.

Table 5: BR($\bar{p}p \to \pi^0\eta$) (4γ final state) measured separately in each data-taking period.

Period	BR($\bar{p}p \to \pi^0\eta$) (10^{-4})
December 1989	1.91 ± 0.14
June 1990	2.05 ± 0.12
July 1990	2.15 ± 0.07
November 1990	2.12 ± 0.07
Unweighted Average	2.06 ± 0.11

4.7 Absolute branching ratios

The total signal strengths and average efficiencies for each reaction are shown in Table 6. To obtain the final branching ratio measurement for each reaction, the signal strengths are combined with the efficiency and the estimated antiproton flux. The results

Table 6: For reactions observed in *zero-prong* trigger data we give γ multiplicity, signal strength, efficiency to observe the final state with given number of γ's, branching ratio for meson decays and $\bar{p}$ flux.

Reaction	N_γ	$N_{observed}$	ϵ_{eff}	Branching Ratio Mesons $\rightarrow \gamma$'s	$\bar{p}$ flux (10^6)
$\bar{p}p \rightarrow \pi^0\eta$	4	9027	0.427	0.389	259.7
$\bar{p}p \rightarrow \pi^0\eta$	8	2491	0.143	0.304	259.7
$\bar{p}p \rightarrow \pi^0\omega$	5	41617	0.350	0.0829	259.7
$\bar{p}p \rightarrow \pi^0\eta'$	4	174	0.372	0.0214	200.9
$\bar{p}p \rightarrow \pi^0\eta'$	8	310	0.157	0.0771	200.9
$\bar{p}p \rightarrow \eta\eta$	4	2708	0.428	0.151	259.7
$\bar{p}p \rightarrow \eta\eta$	8	1450	0.280	0.120	259.7
$\bar{p}p \rightarrow \eta\omega$	5	42588	0.340	0.0326	259.7
$\bar{p}p \rightarrow \eta\omega$	9	9415	0.097	0.0258	259.7
$\bar{p}p \rightarrow \eta\eta'$	4	95	0.348	0.00845	200.9
$\bar{p}p \rightarrow \eta\eta'$	8	211	0.146	0.0303	200.9
$\bar{p}p \rightarrow \omega\omega$	6	11668	0.199	0.00704	259.7
$\bar{p}p \rightarrow \eta'\omega$	5	477	0.170	0.00183	200.9
$\bar{p}p \rightarrow \eta'\omega$	9	1011	0.095	0.00657	200.9

in different final states are then averaged (using as a weight the statistical errors combined with the independent components of the systematic errors). The constant contributions to the systematic errors are then added to the average error, and combined with the error on the antiproton flux. The resulting final branching ratios are given in Table 7. The errors quoted are (in order) the statistical error, the systematic error and the uncertainty in meson branching fractions [37].

5 Relative branching ratios

As well as absolute branching ratios, there is often interest in the ratio of annihilation probabilities for different reactions, or the ratio of the probability of seeing the same reaction in different final states (e.g. to extract η or η' relative widths). We thus calculate several such quantities, where we remove from the calculations the effect of common systematic effects in the measurements.

5.1 The meson decay ratios $\Gamma_{\eta \rightarrow 3\pi^0}/\Gamma_{\eta \rightarrow \gamma\gamma}$ and $\Gamma_{\eta' \rightarrow \gamma\gamma}/\Gamma_{\eta' \rightarrow \pi^0\pi^0\eta}$

Using the number of η mesons observed in the decays into $\gamma\gamma$ and into $3\pi^0$, we determine the ratio of decay branching ratios $\Gamma_{\eta \rightarrow 3\pi^0}/\Gamma_{\eta \rightarrow \gamma\gamma}$. These two decay modes of the η meson are both observed in the three reactions $\pi^0\eta$, $\eta\eta$ and $\eta\omega$, permitting three independent determinations of the ratio of widths.

From the measured number of events in each reaction, and from the MC detection efficiencies, the ratio of partial decay widths is calculated separately for each run period. This permits cancellation of any run dependent uncertainties. A χ^2 test shows that all runs produce compatible results. At this stage we apply the analysis efficiency We then average the values from all runs, using as weight the combined statistical and systematic

Table 7: Absolute branching ratios for reactions measured in the *zero-prong* trigger data (the first error is statistical, the second systematic, the third is the uncertainty in the meson decay branching ratios). Results of previous measurements are also given (note that where available we give measurements rather than upper limits).

Reaction	Our Branching Ratio	Previous Measurements
		$(82 \pm 10) \cdot 10^{-4}$ [33]
$BR(\bar{p}p \to \pi^0\eta)$	$(2.12 \pm 0.08 \pm 0.09 \pm 0.02) \cdot 10^{-4}$	$(4.6 \pm 1.3) \cdot 10^{-4}$ [38]
		$(2.9 \pm 1.5) \cdot 10^{-4}$ [20]
		$(1.33 \pm 0.27) \cdot 10^{-4}$ [21]
$BR(\bar{p}p \to \pi^0\omega)$	$(5.73 \pm 0.22 \pm 0.24 \pm 0.34) \cdot 10^{-3}$	$(23.8 \pm 6.5) \cdot 10^{-3}$ [33]
		$(5.2 \pm 0.5) \cdot 10^{-3}$ [38]
$BR(\bar{p}p \to \pi^0\eta')$	$(1.23 \pm 0.11 \pm 0.05 \pm 0.06) \cdot 10^{-4}$	$(30^{+69}_{-61}) \cdot 10^{-4}$ [33]
		$(5. \pm 1.9) \cdot 10^{-4}$ [38]
$BR(\bar{p}p \to \eta\eta)$	$(1.64 \pm 0.07 \pm 0.07 \pm 0.02) \cdot 10^{-4}$	$(0.81 \pm 0.31) \cdot 10^{-4}$ [21]
		$(1.6 \pm 0.8) \cdot 10^{-4}$ [20]
$BR(\bar{p}p \to \eta\omega)$	$(1.51 \pm 0.06 \pm 0.06 \pm 0.09) \cdot 10^{-2}$	$(0.46 \pm 0.14) \cdot 10^{-2}$ [20]
		$(1.04^{+0.09}_{-0.10}) \cdot 10^{-2}$ [21]
$BR(\bar{p}p \to \eta\eta')$	$(2.16 \pm 0.21 \pm 0.09 \pm 0.11) \cdot 10^{-4}$	
$BR(\bar{p}p \to \omega\omega)$	$(3.32 \pm 0.14 \pm 0.14 \pm 0.28) \cdot 10^{-2}$	$(1.4 \pm 0.6) \cdot 10^{-2}$ [39]
$BR(\bar{p}p \to \eta'\omega)$	$(0.78 \pm 0.05 \pm 0.03 \pm 0.06) \cdot 10^{-2}$	

errors (the only systematic errors used are those particular to each measurement and which cannot cancel in the ratios). The resulting ratios of widths are given in Table 8.

Table 8: Ratio of $\Gamma_{\eta \to 3\pi^0}/\Gamma_{\eta \to \gamma\gamma}$ measured in three reactions.

Reaction	Ratio of widths
$\bar{p}p \to \pi^0\eta$	0.876 ± 0.060
$\bar{p}p \to \eta\eta$	0.855 ± 0.070
$\bar{p}p \to \omega\eta$	0.801 ± 0.050

We then average the three individual results (using the error on each as a weight). This gives as our final result

$$\frac{\Gamma_{\eta \to 3\pi^0}}{\Gamma_{\eta \to \gamma\gamma}} = 0.841 \pm 0.034 \tag{3}$$

which compares favorably with the 'world average' of 0.84 ± 0.06 and the constrained fit result of the Particle Data Group (fitting all η decay branching ratios) of 0.819 ± 0.009 [40].

The η' decays are treated in a similar fashion to give first three separate measurements (see Table 9), and then, by averaging the three separate measurements, the final result:

$$\frac{\Gamma_{\eta' \to \gamma\gamma}}{\Gamma_{\eta' \to \pi^0\pi^0\eta}} = 0.091 \pm 0.009 \quad . \tag{4}$$

This can be compared with another direct measurement of this quantity, $0.112 \pm 0.002 \pm 0.006$ [41], and also to the Particle Data Group constrained fit result of 0.105 ± 0.009 [40].

Table 9: Ratio of $\Gamma_{\eta'} \to \gamma\gamma/\Gamma_{\eta'} \to \pi^0\pi^0\eta$ measured in three reactions.

Reaction	Ratio of widths
$\bar{p}p \to \pi^0\eta'$	0.090 ± 0.018
$\bar{p}p \to \eta\eta'$	0.071 ± 0.019
$\bar{p}p \to \omega\eta'$	0.100 ± 0.012

5.2 The ratio of branching ratios for production of η and η' mesons

The ratios of branching ratios of decays involving η and η' mesons are of interest, as they are sensitive to several physics topics (e.g. the pseudoscalar mixing angle [42]). To determine these ratios as accurately as possible, we use first measurements of the individual branching ratios in final states with the same number of photons and where the data was taken inside just one run period (permitting cancellation of much of the systematic error which is common to both values in any ratio). The resulting ratios of ratios for each γ multiplicity and from each run period are then averaged. The results are thus more accurate than those which can be found by simply taking the ratios of values in Table 7. We find

$$\frac{BR(\bar{p}p \to \pi^0\eta')}{BR(\bar{p}p \to \pi^0\eta)} = 0.548 \pm 0.046 \pm 0.014 \pm 0.028 \quad (5)$$

$$\frac{BR(\bar{p}p \to \eta\eta')}{BR(\bar{p}p \to \eta\eta)} = 1.309 \pm 0.127 \pm 0.032 \pm 0.067 \quad (6)$$

$$\frac{BR(\bar{p}p \to \omega\eta')}{BR(\bar{p}p \to \omega\eta)} = 0.515 \pm 0.028 \pm 0.013 \pm 0.026 \quad (7)$$

$$\frac{BR(\bar{p}p \to \pi^0\eta)}{BR(\bar{p}p \to \pi^0\pi^0)} = 0.303 \pm 0.006 \pm 0.008 \pm 0.003 \quad (8)$$

$$\frac{BR(\bar{p}p \to \eta\eta)}{BR(\bar{p}p \to \pi^0\pi^0)} = 0.232 \pm 0.009 \pm 0.006 \pm 0.003 \quad (9)$$

$$\frac{BR(\bar{p}p \to \pi^0\omega)}{BR(\bar{p}p \to \eta\omega)} = 0.377 \pm 0.005 \pm 0.010 \pm 0.003 \quad (10)$$

where again the first error is statistical, the second systematic and the third from meson branching fractions that do not cancel in the ratios. Note that the result for $\eta\eta'/\eta\eta$ differs by 4 parts per thousand from the value we give in a previous publication [42]. This represents an improvement in the analysis.

Many authors have previously commented on the need for accurate measurements of many of these ratios. Given our new measurement of $BR(\bar{p}p \to \pi^0\pi^0)$, we draw particular attention to ratios involving this quantity. The ratio $\eta\eta/\pi^0\pi^0$ is held to be important as both reactions proceed from the same initial $\bar{p}p$ states $^3P_0$ and $^3P_2$. The effects of initial state interactions are thus minimized. Using a baryon exchange model for the $\bar{p}p$ annihilations it is predicted [2] that $\eta\eta/\pi^0\pi^0 = 0.13$. The same authors also calculate this ratio applying the quark line rule (when annihilation diagrams dominate) and predict $\eta\eta/\pi^0\pi^0 = 1$. (These predictions ignore phase space effects and assume coupling only to the non-strange component of the η). Our measurement of 0.232 ± 0.011 is clearly compatible with neither prediction. Another prediction exists for $\eta\eta/\pi^0\pi^0$ in the case of the quark line rule dominated by annihilation diagrams [7]. In this case the predicted value for $\eta\eta/\pi^0\pi^0$ is 1/4, which is in agreement with our results. In the same paper the ratio $\pi^0\eta/\pi^0\pi^0$

is also predicted. For the case of the quark line rule dominated by rearrangement they find $\pi^0\eta/\pi^0\pi^0 = 1/25$. This does not agree with our data. Thus the latter paper gives a consistent explanation in terms of the quark line rule when rearrangement is negligible. However, this has to be qualified by the contradictory predictions of other authors as shown. We will present a more detailed discussion of the comparison of these ratios with predictions in a future paper (where we will in particular discuss final states containing ω's).

We give these examples of the use of our results to draw attention to the fact that the experimental measurements of these ratios are now sufficiently accurate to permit realistic testing of many models. In particular the new value for BR($\bar{p}p \rightarrow \pi^0\pi^0$) greatly changes ratios involving this quantity, requiring a re-examination of any previous comparisons of such ratios to predictions.

6 Comparison of the measured branching ratios with predictions of models

As outlined in the introduction, there are many open questions related to the process of $\bar{p}p$ annihilation. Various models have been developed which incorporate different assumptions as to the nature of the most important physics involved in these annihilations. Many of the models can be used to predict the two-body branching ratios in $\bar{p}p$ annihilations at rest. In this section we compare our results with the predictions of several typical models.

We choose a selection of recent models. These are: Model A [1], based upon the idea of a nucleon exchange potential including Δ isobars etc. (this work includes variations in the results reflecting choices of parameters describing the effects of initial state interactions, we give the results the authors favour). Model B [3], based upon the use of overlap of protonium wave functions with selection rules and kinematic constraints combined with a minimum transition potential. Model C [11], based upon the importance of quark lines in the $\bar{p}p$ annihilation and subsequent production of a two meson final state (they favour rearrangement of quark lines over the possibility of annihilation of quarks). Finally we choose D [43], where a diquark model for protonium annihilations is assumed (i.e. each nucleon is considered as a diquark plus a more loosely bound quark, the annihilation of two nucleons is then seen as the annihilation of the two diquarks with the two single quarks flowing into the final state where they combine with a $q\bar{q}$ pair formed as a result of the annihilation).

In Table 10 we compare our results with the predictions of the various models. We can see that there is no complete agreement with any model. In particular, for $\bar{p}p \rightarrow \omega\omega$ there is a discrepancy between the measurement and all the models. This reaction can only proceed from the $^3P_0$ and $^3P_2$ initial $\bar{p}p$ states, so the large branching ratio we measure is indeed a surprise. Given the precision of our results, we feel that such discrepancies can no longer be dismissed as due to failings in the experimental measurements, but indicate that the models should either be further developed or the features of several models combined together.

7 Summary

Using the Crystal Barrel detector we have measured a series of branching ratios for $\bar{p}p$ annihilations at rest into two-body final states. In particular we have used our excellent γ detection capability to reconstruct final states containing π^0's and η's. In some cases we have made the first fully inclusive observations of the final state, e.g. $\bar{p}p \rightarrow \omega\omega$ which

Table 10: Comparison of our measured branching ratios with predictions from various models. (Units are 10^{-3})

Reaction	Our Measurement	Model A [1]	Model B [3]	Model C [11]	Model D [43]
$\bar{p}p \to \pi^0\pi^0$	0.693 ± 0.043	0.96	0.9	–	–
$\pi^0\eta$	0.212 ± 0.012	0.14	0.2	–	–
$\pi^0\omega$	5.73 ± 0.47	21.8	42.3	14.0	4.5
$\pi^0\eta'$	0.123 ± 0.013	0.14	0.2	–	–
$\eta\eta$	0.164 ± 0.010	0.15	0.5	–	–
$\eta\omega$	15.1 ± 1.2	1.3	6.7	9.3	14.5
$\eta\eta'$	0.216 ± 0.025	0.42	0.5	–	–
$\omega\omega$	33.2 ± 3.4	16.6	22.8	10.8	4.6
$\omega\eta'$	7.8 ± 0.8	1.1	–	–	7.5

was previously studied [39] using the missing mass technique. Our results are typically of higher precision than previous measurements, or are for final states where previous results were either ambiguous (e.g. $\pi^0\pi^0$, $\eta\omega$) or non-existent ($\eta\eta'$, $\omega\eta'$). We have accurately determined ratios of the rates for many of these reactions. From these results we make direct measurements of η (and η') relative decay widths. In a separate publication [35] we discuss the significance of the magnitude of our measurement of BR($\bar{p}p \to \pi^0\pi^0$), which is larger than previous results, and which at first glance seems to question the assumption that S-wave strongly dominates $\bar{p}p$ annihilation at rest. In another publication [42] we determine the pseudoscalar mixing angle, using the ratios of branching ratios involving any meson recoiling against an η and η' in turn. In a future publication we will examine in more detail the reactions $\bar{p}p \to \pi^0\omega$ and $\bar{p}p \to \eta\omega$, where we will consider the relative importance of quark annihilation and rearrangement diagrams in the reactions. Finally we have presented a comparison of our results with various models for production of two meson final states in the annihilation. We find that none of the models considered provides a full description of the data, and in particular all fail to accommodate the surprisingly large measured rate for $\bar{p}p \to \omega\omega$. This indicates the need for further work in this field.

Clearly, many years after the pioneering work in bubble chambers, there is still great value in the study of branching ratios for $\bar{p}p$ annihilations at low energy.

We would like to thank the technical staff of the LEAR machine group and of all the participating institutions for their invaluable contributions to the success of the experiment. We acknowledge financial support from the German Bundesministerium für Forschung und Technologie, the Schweizerischer Nationalfonds, the British Science and Engineering Research Council and the US Department of Energy (contract No. DE-FG03-87ER40323 and DE-AC03-76SF00098). K. Königsmann acknowledges support from the Deutsche Forschungsgemeinschaft (Heisenberg Programme). S.U. Chung and J. Kisiel benefit from financial support provided by the Alexander von Humboldt Foundation. The Mainz group would like to thank Dr. Renk for the maintenance of the local computer cluster.

References

[1] T. Hippchen, J. Haidenbauer, K. Holinde and V. Mull, Phys. Rev. **C44** (1991) 1337
[2] C. B. Dover, T. Gutsche, M. Maruyama and A. Faessler, Prog. Part. and Nucl. Phys. **29** (1992) 87
[3] S. Mundigl, M. Vicente Vacas and M. Weise, Z. Phys. A – Hadrons and Nuclei **338** (1991) 103
[4] E. Klempt, Phys. Lett. **B244** (1990) 122
[5] C. Dover, J.M. Richard and J. Carbonell, Phys. Rev. **C44** (1991) 1281
[6] T. Hippchen, K. Holinde and W. Plessas, Phys. Rev. **C39** (1989) 761
[7] C. Dover and P. Fishbane, Nucl. Phys. **B244** (1984) 349
[8] M. Kohno and W. Weise, Phys. Lett. **B152** (1985) 303
[9] M. Maruyama, S. Furui and A. Faessler, Nucl. Phys. **A472** (1987) 643
[10] J. Vandermeulen, Z. Phys. C – Particles and Fields **37** (1988) 563
[11] U. Hartmann, E. Klempt and J. Körner, Z. Phys. A – Hadrons and Nuclei **331** (1988) 217
[12] M. Doser *et al.*, Nucl. Phys. **A486** (1988) 493
[13] M. Doser *et al.*, Phys. Lett. **B215** (1988) 792
[14] K. D. Duch *et al.*, Z. Phys. C – Particles and Fields **45** (1989) 223
[15] B. May *et al.*, Z. Phys. C – Particles and Fields **46** (1990) 191,203
[16] J. Reifenröther *et al.*, Phys. Lett. **B267** (1991) 299
[17] P. Weidenauer *et al.*, Z. Phys. C – Particles and Fields **47** (1990) 353
[18] M. Chiba *et al.*, Phys. Rev. **D38** (1988) 2021
[19] L. Adiels *et al.*, Z. Phys. C – Particles and Fields **35** (1987) 15
[20] M. Chiba *et al.*, Phys. Rev. **D39** (1989) 3227
[21] L. Adiels *et al.*, Z. Phys. C – Particles and Fields **42** (1989) 49
[22] E. Aker *et al.*, Phys. Lett. **B260** (1991) 249
[23] C. Amsler *et al.*, Phys. Lett. **B291** (1992) 347
[24] E. Aker *et al.*, Nucl. Instrum. Meth. **A321** (1992) 69
[25] B. Schmid, PhD thesis, pages 21-22. Univ. of Zurich (1991)
[26] R. Brun *et al.*, GEANT 3, Internal Report CERN-DD/EE/84-1, CERN, 1987
[27] A. Janni, Atomic Nuclear Data Tables **27** (1982) 147
[28] W. Bruckner *et al.*, Z. Phys. A – Hadrons and Nuclei **335** (1990) 217
[29] C. Baltay *et al.*, Phys. Rev. Lett. **15** (1965) 532
[30] R. Armenteros and B. French, Antinucleon-nucleon interactions, in High Energy Physics, volume **4**, chapter VI and VII, p. 237–417, (Academic Press, 1968)
[31] G. Smith, Proc. of the Workshop on the Elementary Structure of Matter, Les Houches, France, p. 197, (Springer, 1987)
[32] S. Devons *et al.*, Phys. Rev. Lett. **27** (1971) 1614
[33] G. Backenstoss *et al.*, Nucl. Phys. **B228** (1983) 424
[34] G. Bassompierre *et al.*, Proceedings of 4th European Antiproton Conference, (Bari 1978), volume **I**, p. 139, (pub. Centre National de la Recherche Scientifique, Paris, 1979)
[35] C. Amsler *et al.*, Phys. Lett. **B297** (1992) 214
[36] M. Merkel, PhD thesis, Univ. of Mainz (1992)
[37] Particle Data Group, Phys. Rev. **D45** (1992) S1
[38] M. Chiba *et al.*, Phys. Lett. **B202** (1988) 447
[39] M. Bloch, G. Fontaine and E. Lillestol, Nucl. Phys. **B23** (1970) 221
[40] Particle Data Group, Phys. Rev. **D45** (1992) S VII (Meson Full Listings)
[41] D. Alde *et al.*, Z. Phys. C – Particles and Fields **36** (1987) 603
[42] C. Amsler *et al.*, Phys. Lett. **B294** (1992) 451
[43] A. Cieply, M.P. Locher and B. S. Zou, Diquark Model for Protonium Annihilation into Two Mesons, Paul Scherrer Institute preprint PSI-PR-92-23, accepted for publication by Z. Phys. A – Hadrons and Nuclei

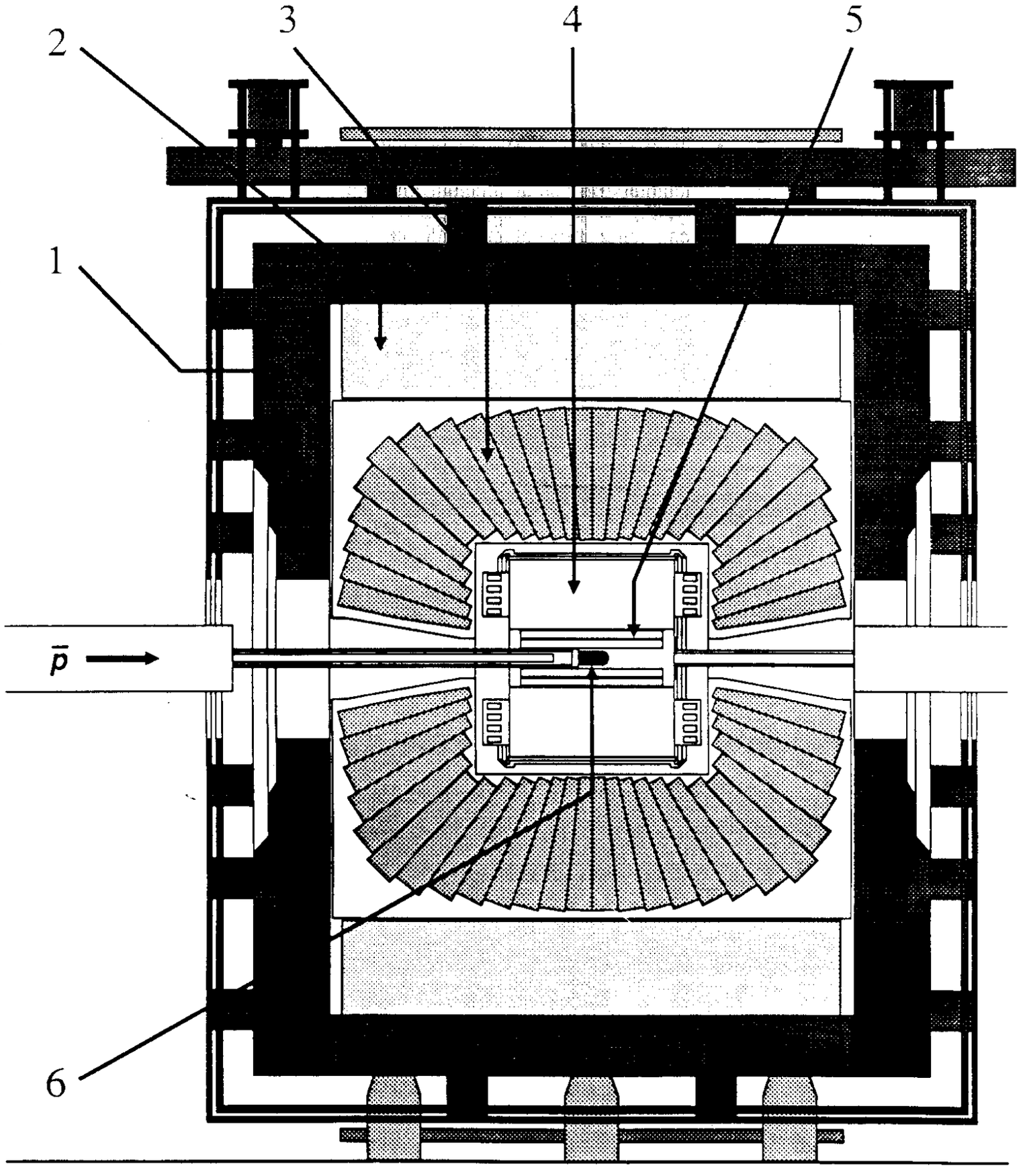

Figure 1: Side view of the Crystal Barrel Detector with 1 Magnet yoke, 2 Magnet aluminium coil, 3 CsI electromagnetic calorimeter, 4 Jet Drift Chamber, 5 Proportional Wire Chambers, and 6 LH_2 target.

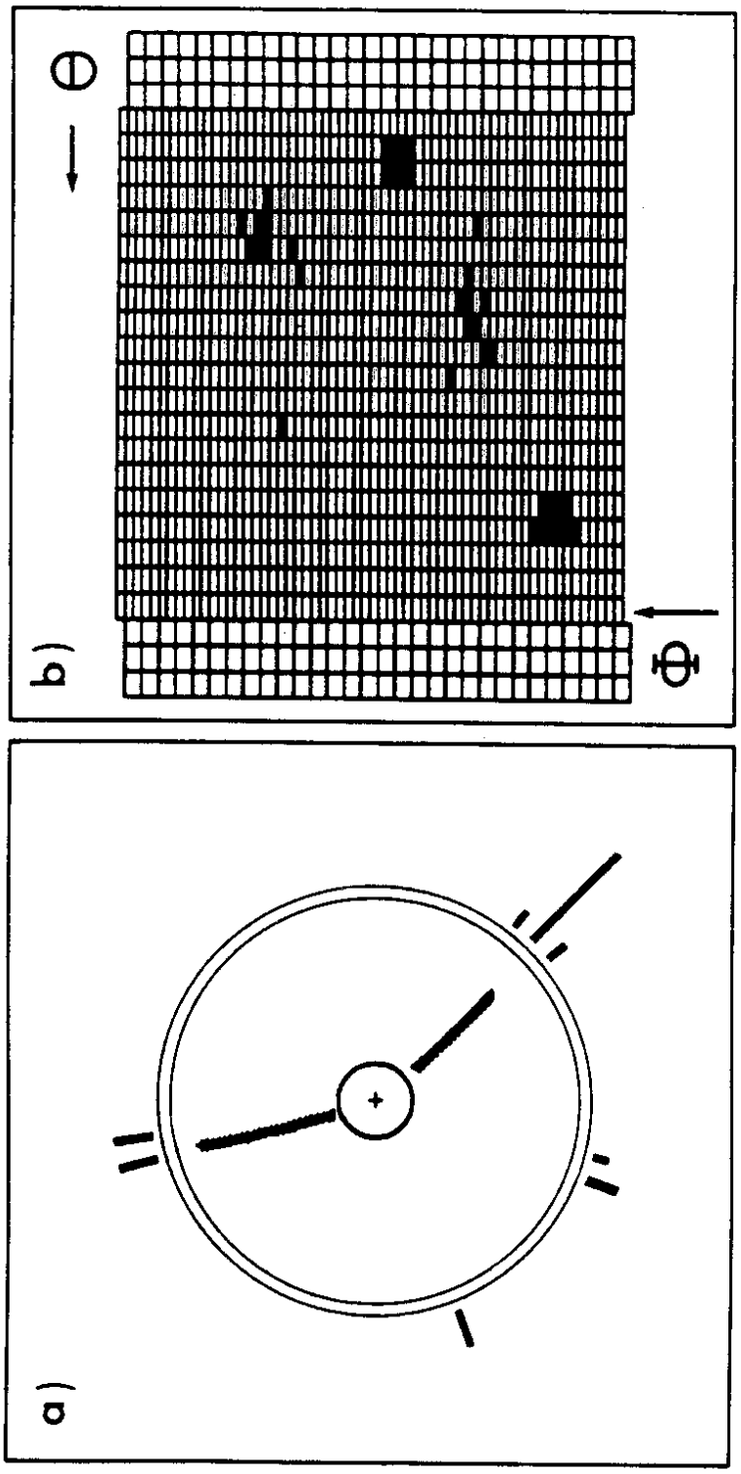

Figure 2: Typical event originating from the reaction $\bar{p}p \rightarrow \pi^+\pi^-\pi^0$ with $\pi^0 \rightarrow \gamma\gamma$. (a) Shows the $r - \phi$ view, with two tracks in the JDC surrounded by energy towers in the calorimeter. The two towers caused by the tracks in the calorimeter are clear, and the two remaining showers are photons whose invariant mass forms a π^0. (b) Shows an unfolded view of the calorimeter. The hit crystals are shaded. The two almost rectangular shaded blocks are the photons, and the two more diffuse signals are from the tracks.

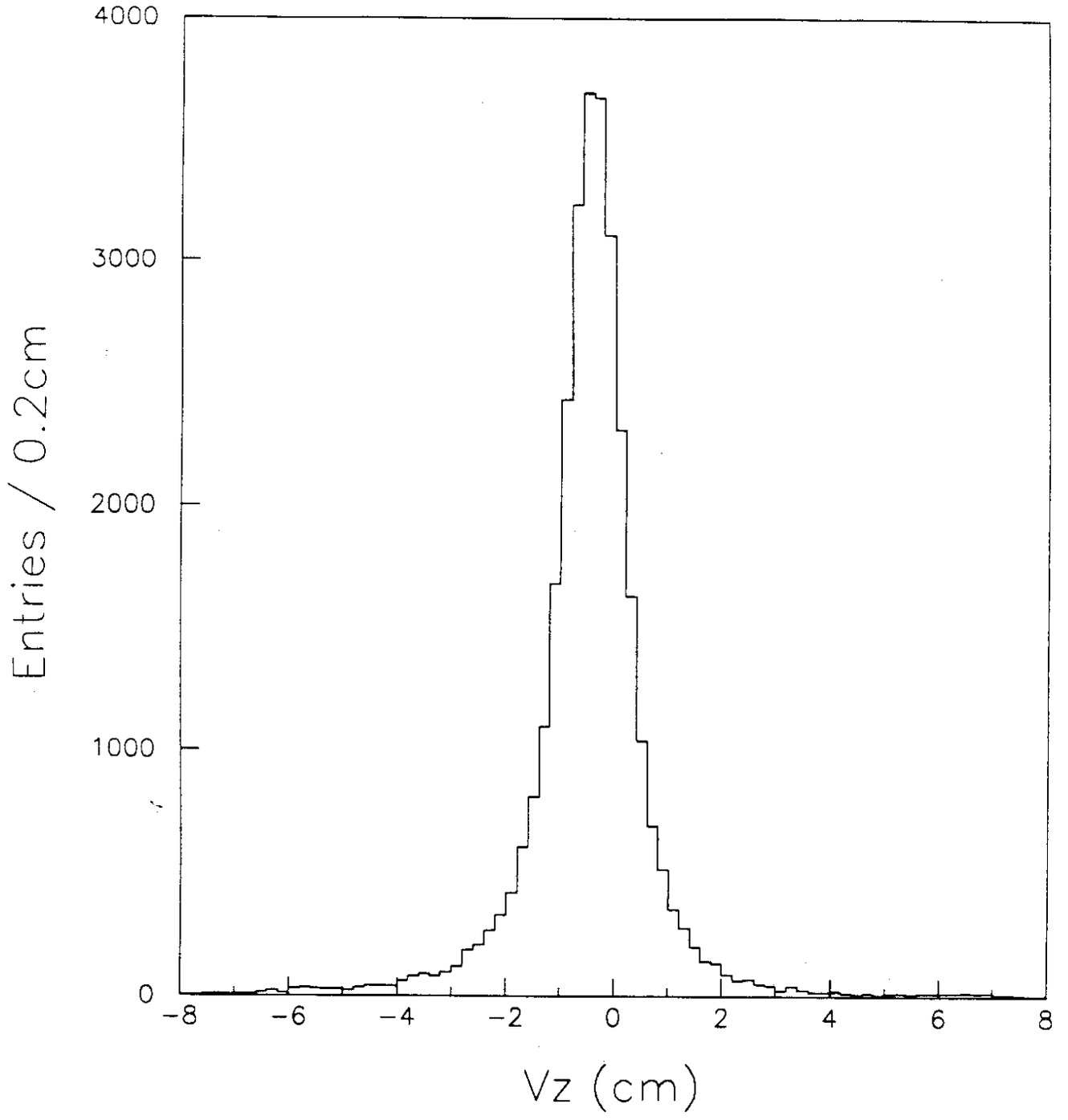

Figure 3: z–projection of the vertex distribution in *open trigger* data.

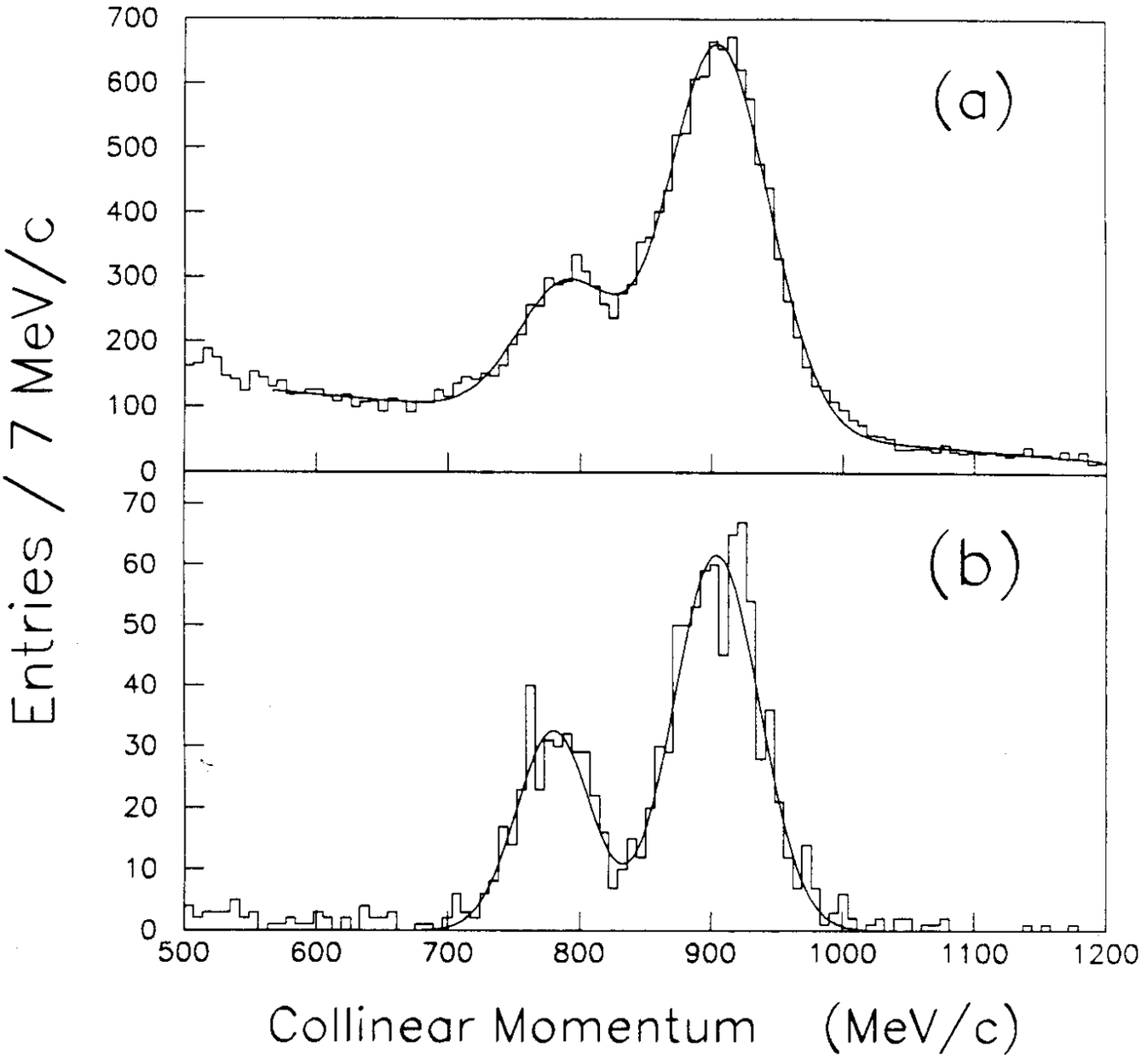

Figure 4: Momentum spectrum for collinear events (one entry per event). (a) Data with standard cuts (b) Specially selected subset of data illustrating JDC resolution.

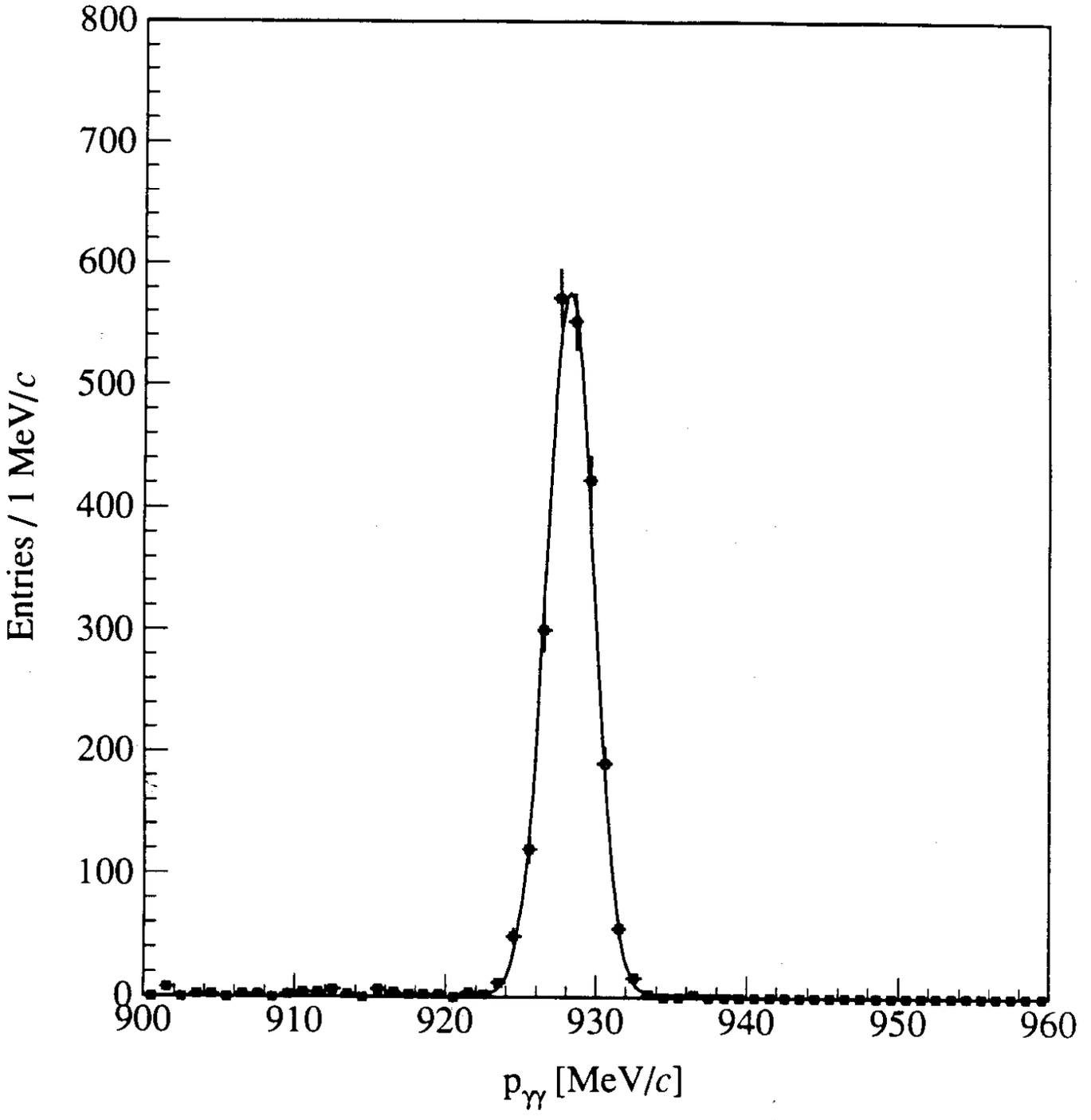

Figure 5: $\gamma\gamma$ momentum spectrum for $\bar{p}p \to 4\gamma$ events in *open trigger* data (six entries per event).

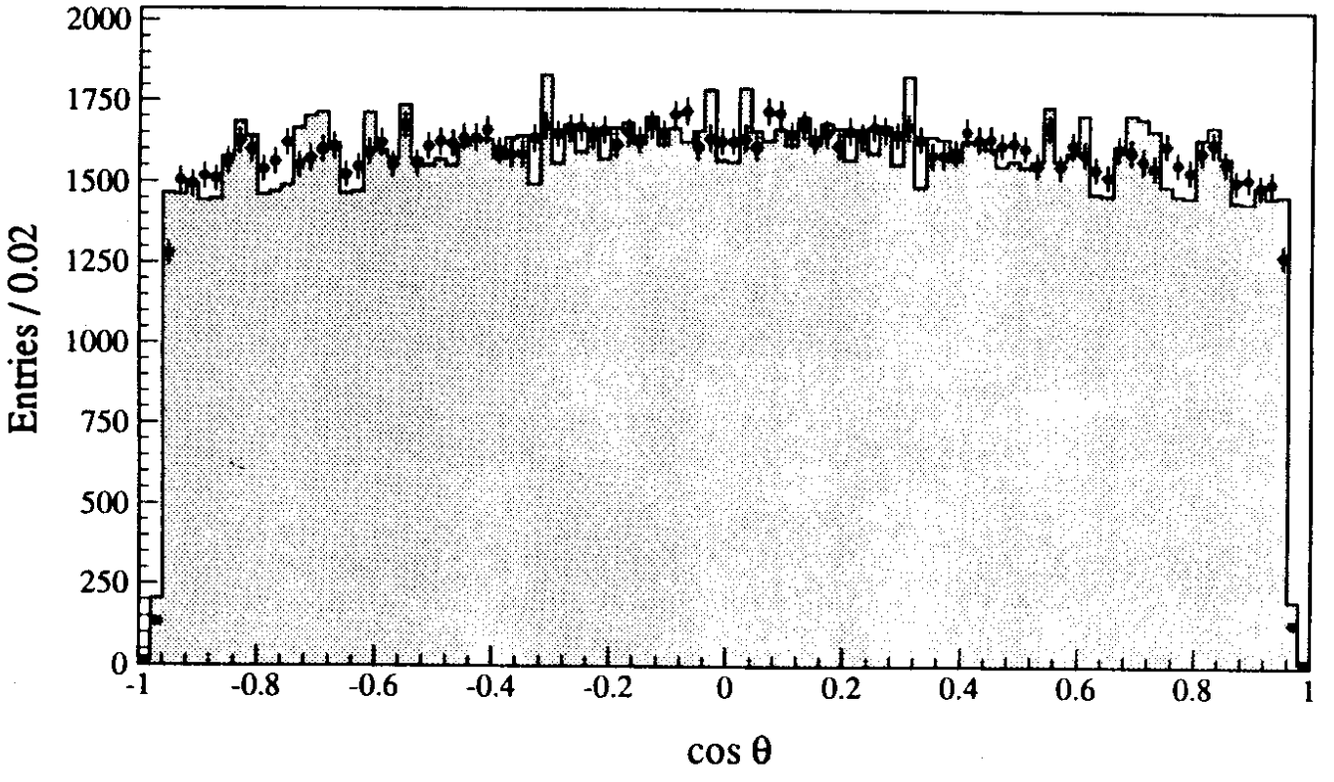

Figure 6: Photon angular distribution in π^0 rest frame. Real data ($\bar{p}p \rightarrow \pi^0\pi^0$) is shown as points, the superimposed histogram is MC data.

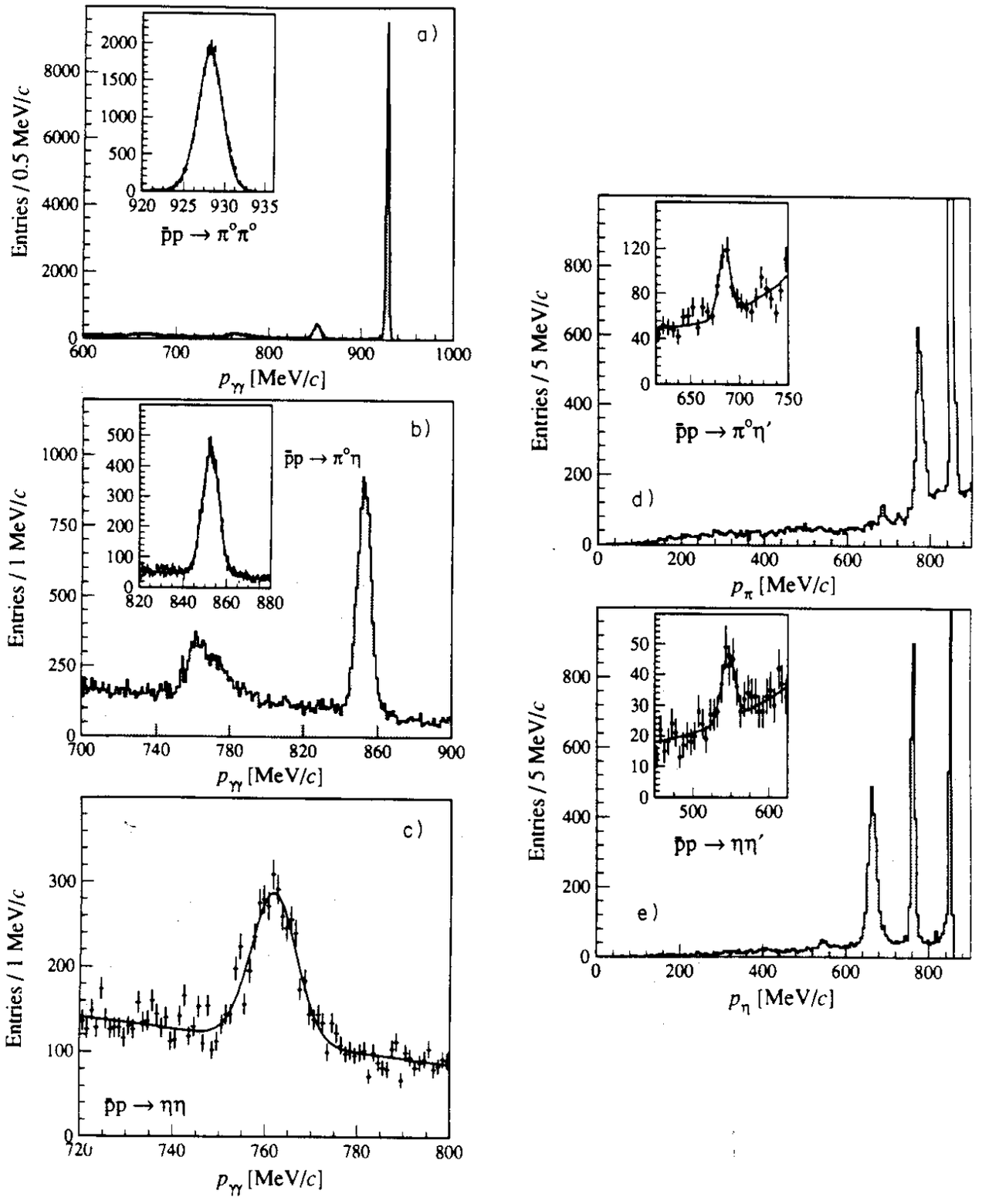

Figure 7: $\bar{p}p \to 4\gamma$ (*zero-prong* trigger data). (a) $\gamma\gamma$ momentum distribution (6 entries per event). (b) Same with suppression of the signal for $\pi^0\pi^0$. (c) Same as (b) where the $\gamma\gamma$ pairs have an invariant mass greater than 200MeV/c^2. (d) Momentum of π^0 in $\bar{p}p \to \pi^0\gamma\gamma$. (e) Momentum of η in $\bar{p}p \to \eta\gamma\gamma$. Insets show fits to the signals.

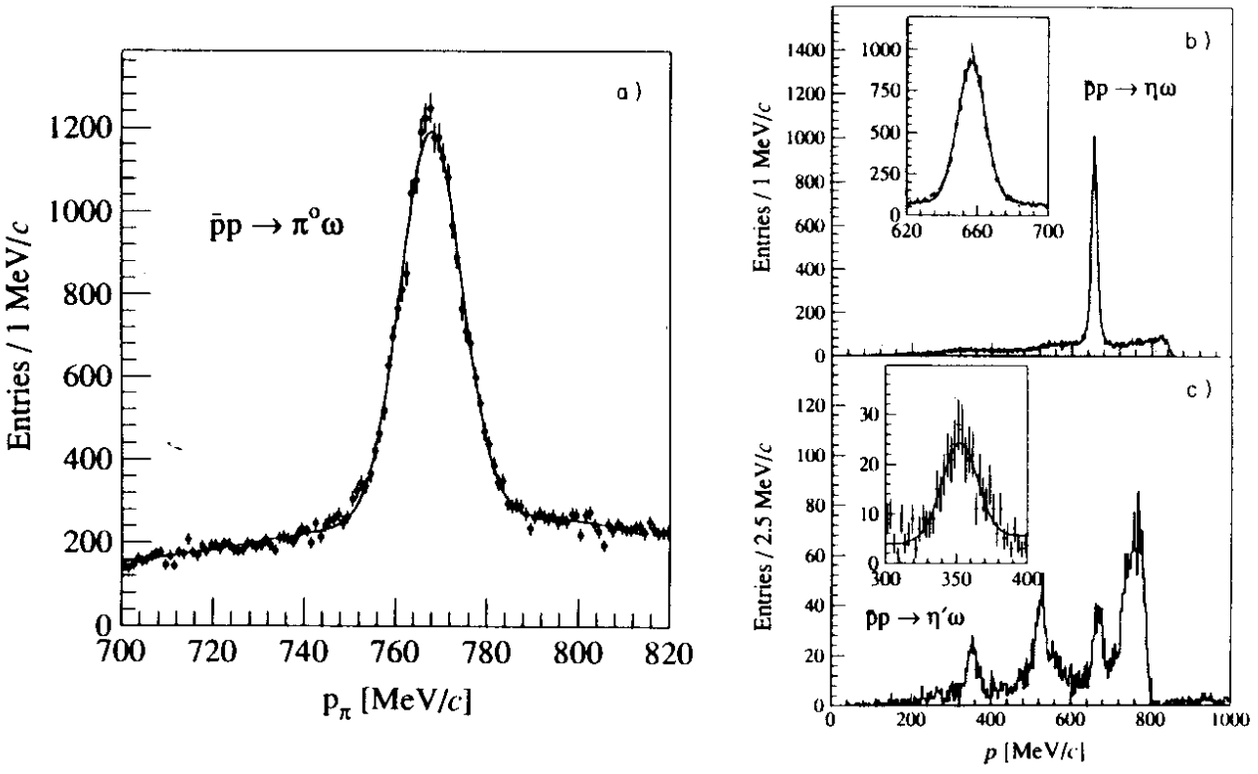

Figure 8: For 5γ events (a) the π^0 momentum in $\pi^0\pi^0\gamma$, (b) the η momentum in $\pi^0\eta\gamma$ and (c) the $\gamma\gamma$ momentum in $\pi^0 3\gamma$(when the recoiling $\gamma\pi^0$ forms an ω). Fits are shown inset.

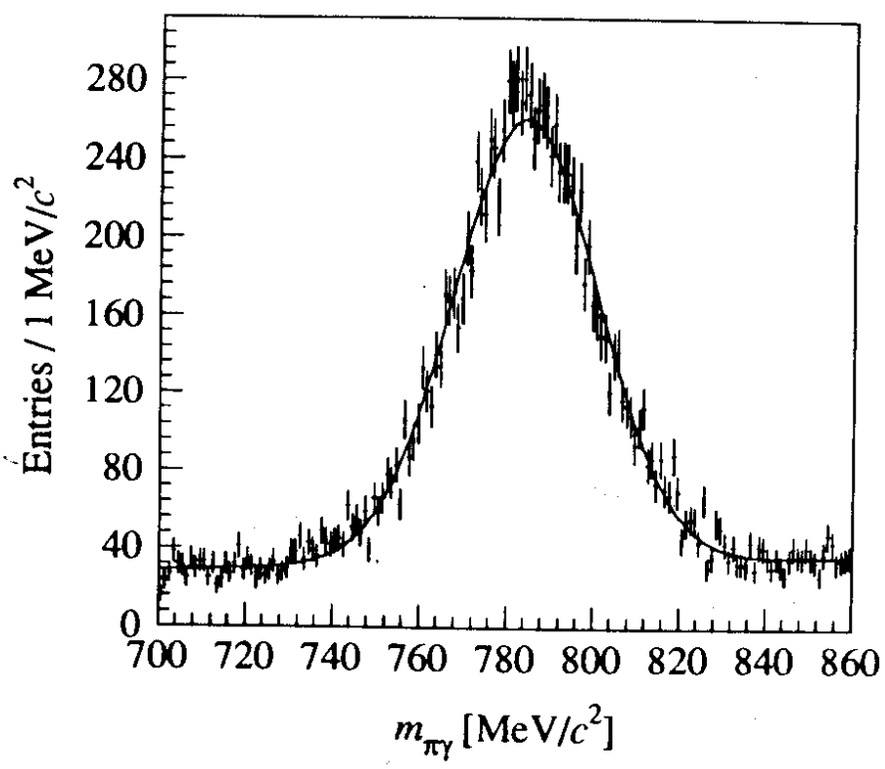

Figure 9: $\gamma\pi^0$ mass recoiling from a ω meson in $\bar{p}p \to \pi^0\pi^0\gamma\gamma$.

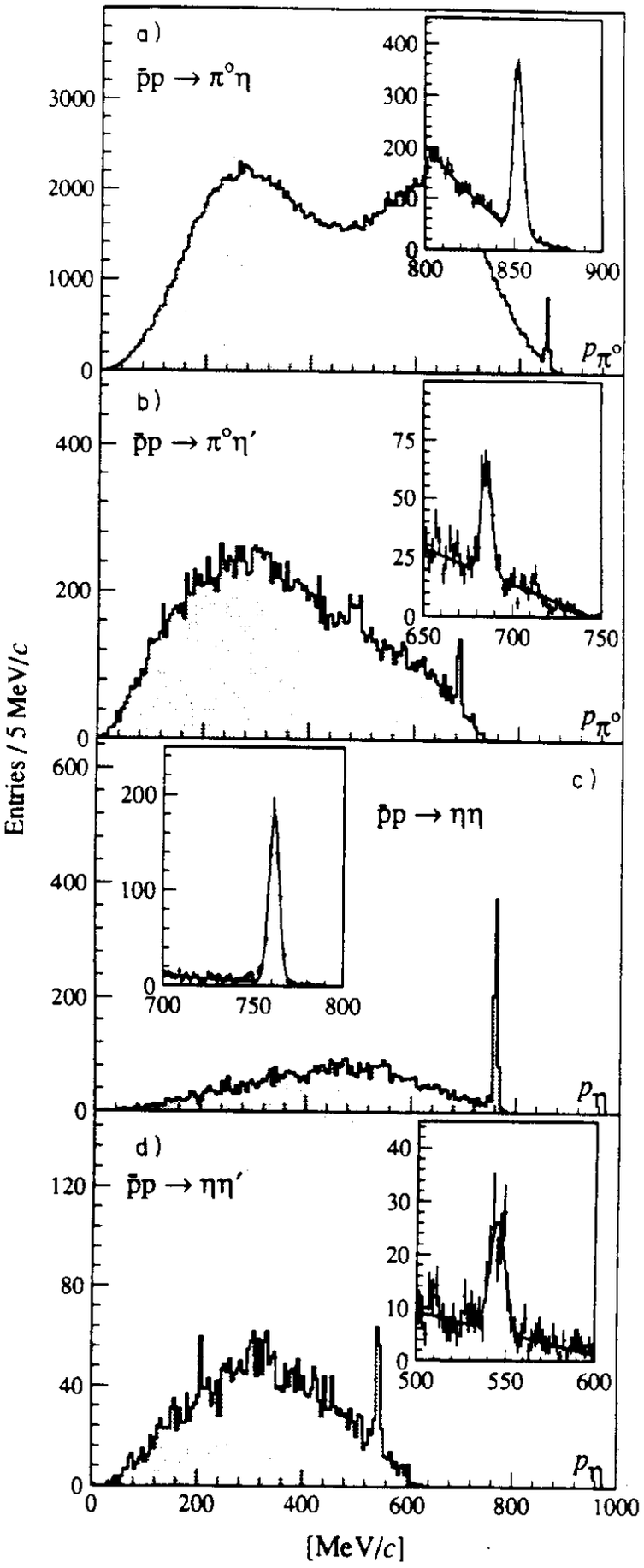

Figure 10: (a) π^0 momentum in $\bar{p}p \to \pi^0\pi^0\pi^0\pi^0$. (b) and (c) are respectively the π^0 and η momenta in $\bar{p}p \to \pi^0\pi^0\pi^0\eta$. (d) η momentum in $\bar{p}p \to \pi^0\pi^0\eta\eta$. Fits are shown inset.

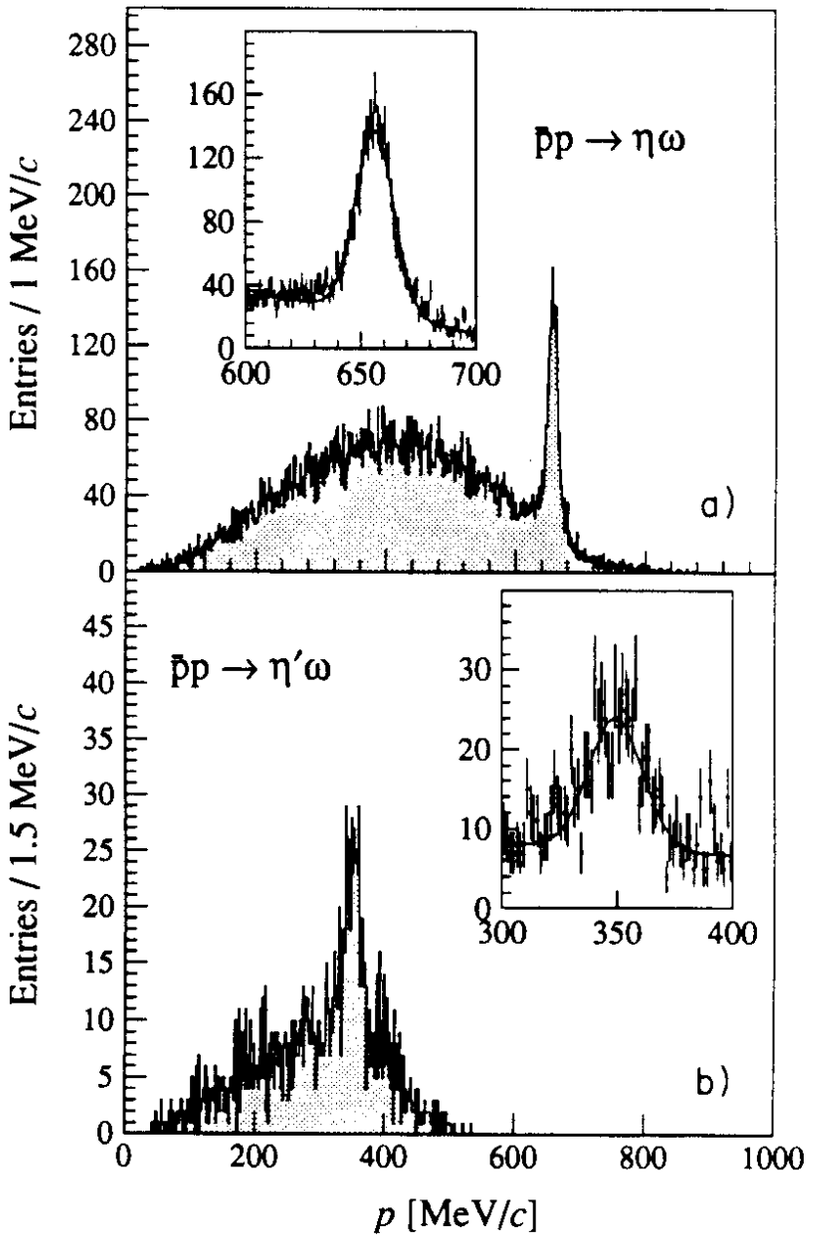

Figure 11: ω momentum in (a) $\bar{p}p \to \pi^0\pi^0\pi^0\pi^0\gamma$ and (b) $\bar{p}p \to \pi^0\pi^0\pi^0\eta\gamma$. Fits are shown inset.